

令和元年度

博士論文

**Study on effects of electric field  
on optical electron-spin injection  
into InGaAs quantum dots**

**Hang Chen**

DIVISION OF ELECTRONICS FOR INFORMATICS  
GRADUATE SCHOOL OF INFORMATION SCIENCE AND TECHNOLOGY  
HOKKAIDO UNIVERSITY

AUGUST 19, 2019



# Acknowledgments

When this paper is completed, I sincerely appreciate my supervisor, Professor Akihiro Murayama, for his instruction, discussions, and supports. High levels of research that Professor Murayama required in academic research have had a great impact on me. Discussions with him about experimental results gave me clear physical images to interpret and understand the phenomena.

I am very grateful to Professor Kazuhisa Sueoka for his valuable discussion on my sample fabrication, and scholarship application. I also appreciate Associate Professor Hirotake Sugawara for his daily care in our office. I would like to thank Assistant Professor Satoshi Hiura, Dr. Agus Subagyo, Dr. Neng Lv, Mr. Junichi Takayama, and Ms. Yukari Kouketsu, for their contributions in measurements. I thank all other students of the Laboratory of Electronic and Photonic Materials for their supports, directly or indirectly to my research.

Finally, I would like to thank my family for their supports and encouragements.



# Contents

Acknowledgments . . . . .	iii
<b>1 Introduction</b>	<b>1</b>
1.1 Semiconductor quantum structures . . . . .	1
1.2 Background of spintronics . . . . .	4
1.3 Generation of carrier-spin polarization . . . . .	11
1.4 Spin polarization detection by light . . . . .	15
<b>2 Research Purpose</b>	<b>17</b>
2.1 Spin injection into QDs . . . . .	17
2.2 Spin injection in QW/QDs coupled nanostructures . . . . .	19
<b>3 Experimental Procedures</b>	<b>22</b>
3.1 Layered QD-based sample and device structures . . . . .	22
3.2 Optical measurement . . . . .	24
<b>4 Efficient electron-spin injection into QD by electric field application</b>	<b>27</b>
4.1 Excitation light power dependence . . . . .	27
4.1.1 QD-PL behavior . . . . .	27
4.1.2 Circularly polarized QD-PL spectra . . . . .	31
4.1.3 CPD value of QD-PL . . . . .	32

4.1.4	Circularly polarized time-resolved QD-PL . . . . .	33
4.2	Effect of tunneling barrier thickness . . . . .	37
4.3	Resonant tunneling and oscillation behaviors of the PL intensity . . .	40
4.3.1	Resonant tunneling induced by wetting layer and LO-phonon emission . . . . .	40
4.4	Summary . . . . .	44
<b>5</b>	<b>Electric-field effects on spin-injection polarity and the spin- polarization degree in QD</b>	<b>46</b>
5.1	Electric-field effects on electron-spin polarity during spin injection . .	46
5.1.1	Excitation-power dependence of CPD property . . . . .	51
5.2	Effects of $p$ -doping in QDs . . . . .	53
5.2.1	Effects of $p$ -doping on QD-PL intensity . . . . .	53
5.2.2	Effect of $p$ -doping on circular polarization property of PL . .	54
5.3	Summary . . . . .	55
<b>6</b>	<b>Conclusion</b>	<b>58</b>
	<b>Bibliography</b>	<b>60</b>
	<b>A Publication</b>	<b>72</b>
A.1	Paper Publication . . . . .	72
A.2	International conference . . . . .	72
A.3	Domestic conference . . . . .	73

# Chapter 1

## Introduction

### 1.1 Semiconductor quantum structures

In nanometer-scale solid-state materials such as semiconductors, quantum effects will be observed [1, 2]. One of the most significant quantum effects is a confinement effect for an electron. An electron can be confined in low dimensional systems when the dimensions of the material are sufficiently small compared to the de Broglie wavelength of the electron.

In 3-dimensional (3D) systems, put electrons into a box with a volume  $\Omega = L_x \times L_y \times L_z$ . The electrons are traveling in each direction with periodic boundary conditions. The corresponding normalized electron states can be expressed by a wavefunction  $\phi_{lmn}$ , as follows:

$$\phi_{lmn}(\mathbf{R}) = \frac{1}{\sqrt{L_x L_y L_z}} \exp[i(k_x x + k_y y + k_z z)] = \frac{1}{\sqrt{\Omega}} \exp(i\mathbf{K} \cdot \mathbf{R}), \quad (1.1)$$

where

$$\mathbf{K} = \left( k_x, k_y, k_z \right) = \left( \frac{2\pi l}{L_x}, \frac{2\pi m}{L_y}, \frac{2\pi n}{L_z} \right), \quad l, m, n = 0, \pm 1, \pm 2, \dots \quad (1.2)$$

A quantum well (QW) is a thin layer of solid-state material, which is sandwiched between other materials as shown in Fig. 1.1 (a). The band-gap energy of the QW with a thickness of  $d_z$  is assumed to be lower than that of the surrounding material ( $d_z \ll L_z, L_y$ ). The electron's motion is unconfined within the  $x, y$ -directions in the QW and confined only in the  $z$ -direction. Therefore, the total electron energy in the QW is the sum of the electron energy along the quantized  $z$ -direction and the other  $x, y$ -directions:

$$E_{tot} = E_z + E_{x,y} = \frac{\hbar^2}{2m^*} \cdot \frac{\pi^2}{d_z^2} \cdot n_z^2 + \frac{\hbar^2}{2m^*} \cdot (k_x^2 + k_y^2), \quad n_z = 1, 2, 3, \dots, \quad (1.3)$$

where  $n_z$  is an integer, and  $m^*$  is the effective mass of the electron.

Each state of the electron is defined based on each wavefunction. The density of the states (DOS) of an electron confined in the QW [shown in Fig. 1.2 (a)] can be written as:

$$\text{DOS}_{2D} = \frac{m^*}{\pi \hbar^2} \sum \Theta(E - E_n), \quad (1.4)$$

where  $\Theta$  is a Heaviside step function. The basic energy dependence of the DOS in a QW with a specific  $d_z$  is constant for the energy due to the quantum confinement.

Quantum dots (QDs) are man-made droplets with the size of less than several tens of nanometers ( $d_{x,y,z} = d$ ) as shown in Fig. 1.1 (b). Electrons are confined for all three dimensions. The total energy of the electron in the QD becomes:

$$E_{tot} = E_l + E_m + E_n = \frac{\hbar^2}{2m^*} \cdot \frac{\pi^2}{d^2} \cdot (n_x^2 + n_y^2 + n_z^2), \quad n_{x,y,z} = 1, 2, 3, \dots, \quad (1.5)$$

where  $l, m$ , and  $n$  are integers. The density of the states [shown in Fig. 1.2 (b)] in the QD is a series of Delta-functions [ $\delta(E)$ ]:

$$\text{DOS}_{0D} = \sum_{l,m,n} \delta(E - E_{l,m,n}), \quad (1.6)$$

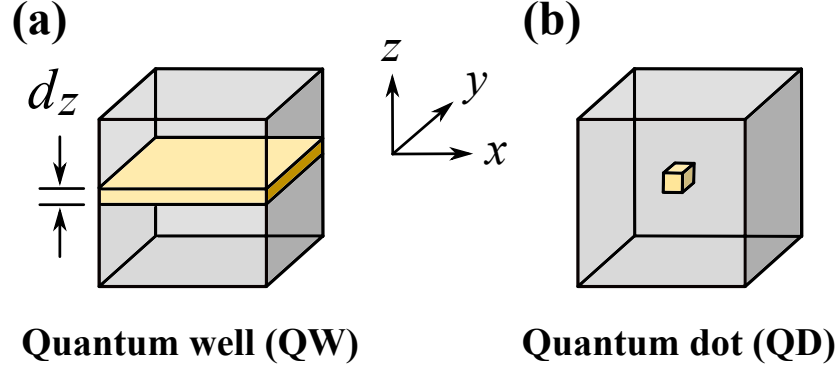


Figure 1.1: Schematic illustrations of (a) a QW and (b) QD, embedded in barrier materials (grey color).

The Pauli exclusion principle for multiple electrons (fermions) forbids from occupying the same state simultaneously [2]. The occupation is statistically governed by the Fermi-Dirac distribution function  $f(E, E_F, T)$ . It is given by:

$$f(E, E_F, T) = \left[ \exp\left(\frac{E - E_F(T)}{k_B T}\right) + 1 \right]^{-1}, \quad (1.7)$$

where  $k_B$  is the Boltzmann's constant.  $E_F$  is called as the *Fermi level* and it varies slightly with a temperature of  $T$ . The Fermi-Dirac function is plotted at a certain temperature in Fig. 1.2 as a black curve.

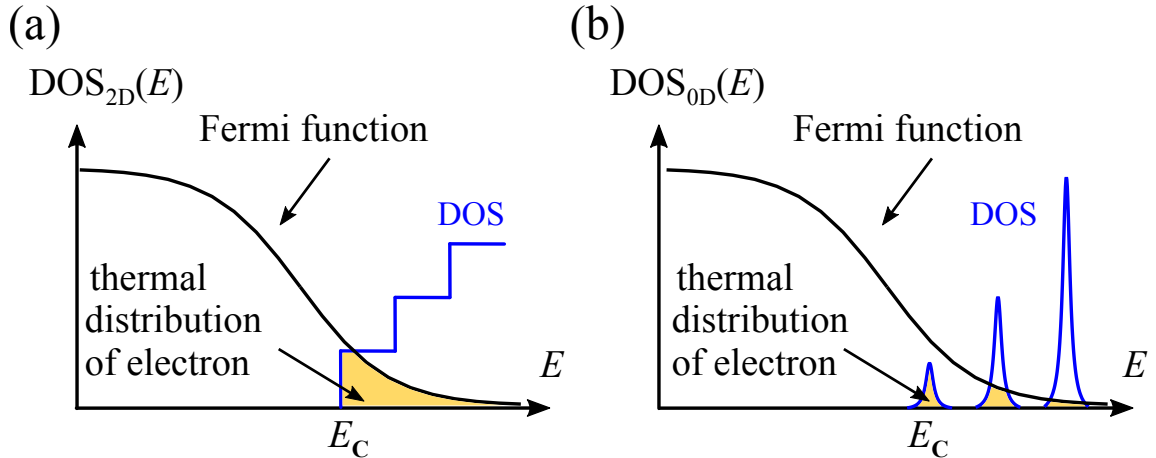


Figure 1.2: The density of the states (DOS) of electrons in a QW (a) and QD (b) (blue line). The DOS of QD is expressed taking the slight size distribution into account. The thermal distribution is given as a black curve. The yellow regions indicate the thermal distribution of electrons.

## 1.2 Background of spintronics

Spintronics, as its name implies, is a technology that studies how to exploit the spin and charge degrees of freedom of electrons to add new performances in electron devices [3,4]. As shown in Fig. 1.3, electronics used previously the freedom of ‘charge’ only. Nowadays, spin-polarized currents or internal electric fields can be used to regulate the electron-spin orientation in solids, adding the ‘spin’ degrees of freedom in electron devices, presenting many new physics effects and opening up new spin-functional devices.

The degree of the freedom of spin was predicted by the Dirac equation. The electron or hole must have an intrinsic angular momentum (or ‘spin’). The spin has two orientations along an external magnetic field: parallel to the field direction (or ‘spin up’), and anti-parallel to the field one (or ‘spin down’).

In this research area, this degree of spin freedom is expected to play important roles in realizing new functions in future electron devices. Conventional electron devices can control the flow of charge only. The spintronic device can control the spin-dependent current or light within the device, thereby adding extra information of spin (Fig. 1.3). Spintronic devices can be realized by employing at least one of the spin-related phenomena, such as injection [5,6], manipulation [7], and detection of the electron spin [8]. Because the spin direction of an electron can be switched from one state to another immediately with extremely low energy consumption. These new values cannot be obtained by conventional electron devices. Up to now, therefore, spintronics opens up new types of device, such as a spin-field-effect transistor (Spin-FET) [9], spin interference device [10], and qubit information readout device [11].

However, the transport of spin-polarized carriers without a significant loss of spin, the optimization of an electron spin lifetime, and the fast manipulation of spin are the major challenges to be solved in the spintronics.

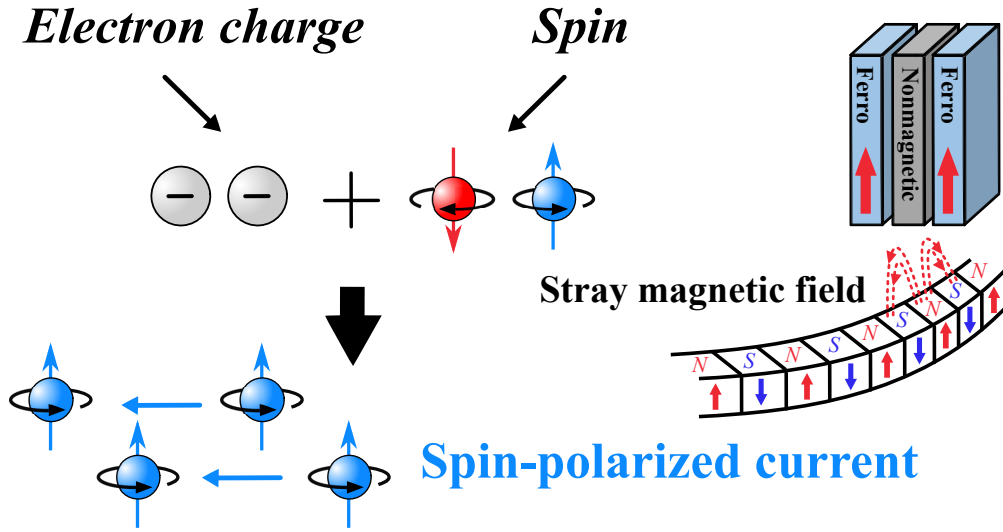


Figure 1.3: Conceptual schematic illustration: spintronics.

The giant magnetoresistance (GMR) [12–14] discovered by Fert [15] and Grünberg [16] in 1988 corresponded to the starting point of spin-based electronic devices. The giant tunnel MR (TMG) by Miyazaki [17] was then used for hard disk drive (HDD) heads. The high-sensitivity detection of a magnetic field using this TMR was applied to a read-head for extremely weak magnetic fields, originating from sub-micron scale magnetized domains as an information memory in HDD. Nevertheless, the concept of ‘spintronics’ was not used by Wolf for the first time until 1996 [18, 19]. Nowadays, electron devices are becoming much more integrated and smaller, which makes spintronic devices one of the most desirable candidates for the next generation electron device because of the ultra-low energy consumption performance owing to the non-volatile property of magnetization. The research field of spintronics is very extensive, and it intersects interestingly with metal and semiconductor material physics, superconducting, mesoscopic, and cold atom physics.

Until now, spintronic devices have been studied in nearly three decades. Awschalom et al. divided the spintronics history into three stages according to the development of the device [3, 20]. The main results of the first stage are the

discovery and application of various MR effects, including the GMR and TMR, mentioned above [15]. In 1993, Helmut measured in rare-earth manganese oxides with perovskite-like structures. The colossal magnetoresistance (CMR) effect [21] and the TMR were found in tunnel junction structures [17,22,23]. Systems exhibiting the GMR typically include two ferromagnetic layers. As shown in Fig. 1.4 [12], one assumes that two ferromagnetic layers are antiferromagnetically coupled without an external magnetic field, and the magnetizations are oppositely (anti-parallel) oriented so that the electrical system is in a higher magnetoresistance state (b). The spin-polarized electrons will be scattered by the magnetization with the anti-parallel configuration for the electron spin. When a magnetic field is applied and its strength is greater than a coercive field of the ferromagnetic layer, one of the magnetizations will be reversed from anti-parallel to parallel to the applied field direction. Therefore, both orientations of the magnetization in the two ferromagnetic layers become identical, and the system is in a lower magnetoresistance state (a) [15]. It is worth noting that the basic principle of the above MR effect is also the basis of the design of more convenient spin valves [24] in the next stage [3]. At this stage, spintronic devices fabricated based on the above MR effects have been successfully applied to the HDD head.

Mott [25] first presented a two spin-current model to explain the GMR. One can assume a resistance  $R_{AP}$  is high for spin-polarized electrons with the antiparallel magnetization direction due to strong electron scattering. A resistance  $R_P$  is lower than  $R_{AP}$ , with the parallel magnetization direction. In the left-hand case in Fig. 1.4 (a), the magnetization is aligned parallel each other. The resistance of the spin-up channel is low, whereas the resistance of the spin-down channel is much higher due to significant scattering. Consequently, the left-hand circuit has a low total resistance. In the right-hand case, Fig. 1.4 (b), the resistances through both spin channels are identical. Therefore, the resistance of the right-hand circuit is higher than that of the

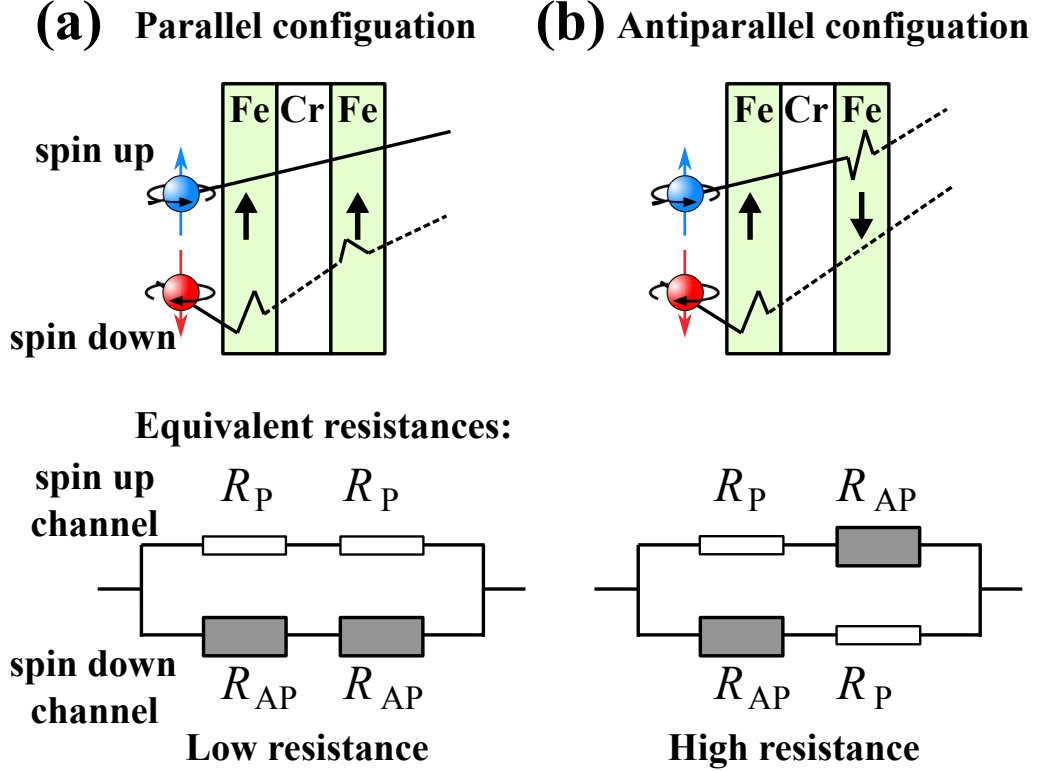


Figure 1.4: A basic scheme of GMR: (a) In the parallel magnetization configuration, one spin-polarized current easily can flow through the device, leading to the lower electrical resistance. (b) By contrast, in the antiparallel magnetization configuration, the total resistance is higher. A two-current circuit model expressing the equivalent resistances of GMR is shown below, corresponding to the above situations (a) and (b), respectively [12].

left-hand circuit. The states with high and low resistances can be switched between the antiparallel and parallel magnetization alignments by application of an external magnetic field [26].

The second stage is in spintronics devices, where it is desirable to use spin-polarized currents instead of conventional spin-independent currents to create spin transistors, spin valves, etc. Thereby, the optical and electrical signals are amplified, and then can be switched by electric field applications for a programmable micro-processor. For this second stage, the theoretical design includes spin-FET (such as Datta-Das type transistors [9], magnetic  $p-n$  junction diodes [27], unipolar spin transistors [28], and magnetic bipolar transistors [29]). Although many design schemes

have been proposed theoretically and some progress has been made in experiments, the spintronic devices designed in this stage are still far from an industrial application.

Here, the Datta-Das transistor [9] is considered at the beginning of this second stage. The original model of the Datta-Das transistor is shown in Fig. 1.5 and is a quasi-two-dimensional system. The left and right ends of the device are a source and drain electrode made of a ferromagnetic material, and respectively performing injection and detection of spin-polarized currents. The middle part is a conducting channel, in which the Rashba spin-orbit coupling is introduced and regulated by a gate voltage (destruction system for interface inversion symmetry) [30–34]. Spin-polarized electrons enter the conductor path from the source electrode, and this spin-polarization produces precession under the effective magnetic field owing to the spin-orbit coupling. When the electron reaches to the drain electrode, if the spin polarization is parallel to that of the magnetic drain, this circuit is turned ‘ON’ [Fig. 1.5 (a)]. Otherwise, the electron is scattered with the anti-parallel configuration at the interface of the drain electrode, then this circuit is turned ‘OFF’ [Fig. 1.5 (b)]. The current switching of the circuit can be controlled by regulating the spin-orbit coupling in the conducting path. Although this Datta-Das transistor model is very attractive, it is not easy to realize, experimentally [35–37]. However, the Datta-Das transistor involves important issues such as spin injection, spin diffusion, and spin relaxation [38–40].

Here is another important application of spintronic devices in this stage. The polarization of photons can also be controlled during a photoelectric conversion process, which is called as a spin-polarized light-emitting diode (spin-LED) as shown in Fig. 1.6 (a) [6, 19, 41–46]. In this device, spin-polarized electrons (or holes) are injected into a QW active region of the device, where they can emit photons with a left-handed or right-handed circular polarization depending on the electron-spin direction. This direct relation between the electron spin and the photon polarization

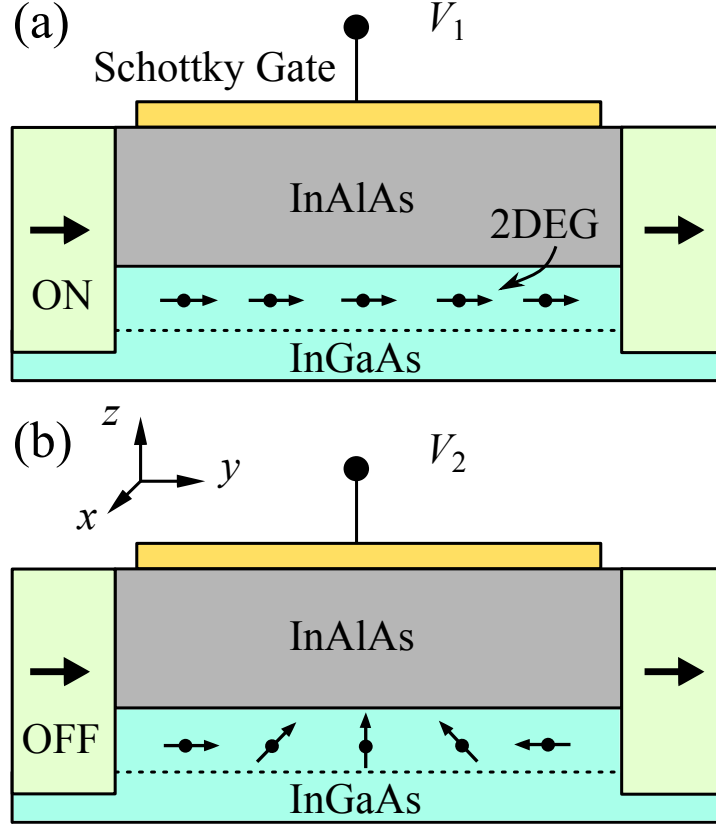


Figure 1.5: Scheme of the Datta-Das spin field-effect transistor. The left source and right drain electrodes made of ferromagnetic metals or semiconductors can realize the injection and detection of spin polarization. The middle part is the 2D-Electron Gas (2DEG) channel, in which the Rashba spin-orbit coupling is introduced and regulated by the gate voltage. In the case of  $V_1$  and  $V_2$ , the circuit can be turned on (a) and off (b), respectively [9, 19].

has many practical possibilities. For example, a circularly polarized light can be used to directly detect the electron spin state in a semiconductor heterojunction as shown in Fig. 1.6 (b). Thereby, the spin-LED promotes to develop spintronics due to their ability to quantify the spin injection process and the resultant spin state.

The Faraday geometry is usually used to detect the spin state owing to the optical selection rule [42, 47, 48]. At present, the spin injection source used is composed of a ferromagnetic material (FM). A spin state with the higher occupancy rate is called as a spin majority state, and the opposite case is a spin minority one. Unfortunately, the process of spin injection into the semiconductor is rather complicated and many

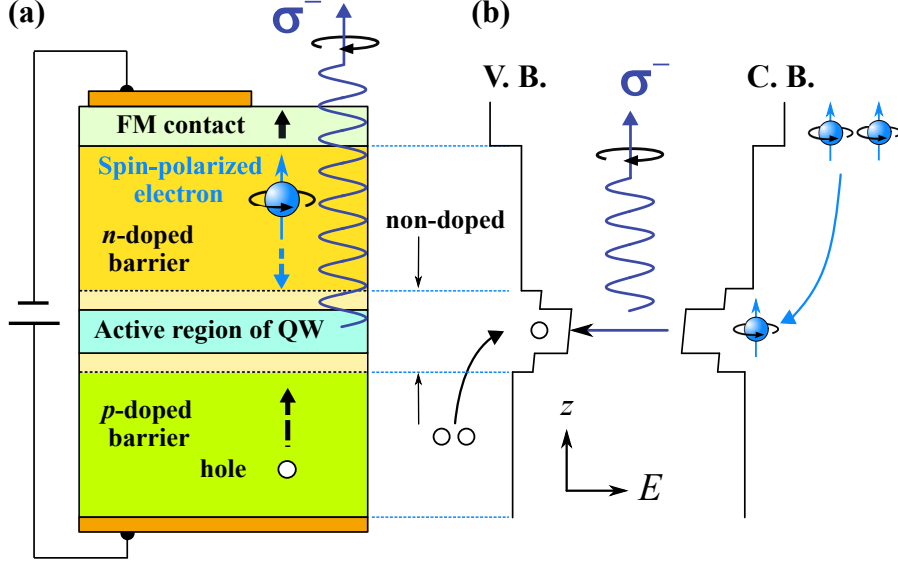


Figure 1.6: (a) Schematic representation of a spin-polarized LED structure with the Faraday geometry. (b) The corresponding band-structure is sketched. Spin-polarized electrons are injected into a QW active region from a top ferromagnetic metal (FM) contact with perpendicular magnetization [47]. Then, circularly polarized light emissions can be induced owing to the optical selection rule.

factors can affect the spin injection efficiency, such as interface material quality, a defect or impurity density, and the interface band structure. How to improve spin-conserving injection efficiency is a big challenge for material growth and energy-band engineering.

The third stage is based on the operation of single or several electron spins, and one hopes to achieve quantum computing, quantum encryption, data compression, and quantum communication [49]. The task at this stage is to combine spin states with quantum information and computing. Three important issues need to be addressed in this area: first, how to extend the spin energy relaxation (direction for the quantized axis) and the spin-phase relaxation (decoherence) times. Second, how to effectively manipulate the spin direction. Third, implemented spintronic devices are requested to have good scalability. In response to these problems, a semiconductor QD system is a good candidate for realizing quantum information and computation using spins, which has a quantized level and a long spin-decoherence time [50, 51]. Besides, QD systems

can take an advantage of existing mature semiconductor micro-nano technologies to facilitate large-scale integration [52]. However, totally speaking, the third stage is still at a relatively early stage, and it takes a long way to achieve solid-state quantum computing.

In the last decade, spintronics has developed rapidly due to advances in the use of optical and electrical methods for spin operations of electrons [53, 54]. Among them, on a time scale (a spatial uniform system) and spatial scale (spin diffusion and transport one), the spin relaxation in various materials under various conditions (such as external field, temperature, doping concentration, and stress) are studied. Moreover, the nature of decoherence is still a major research topic [3, 4, 19, 55].

### 1.3 Generation of carrier-spin polarization

The generation and manipulation of spin polarization are prerequisite for the development of spintronics. Generation of the spin polarization creates a nonequilibrium spin population. The main method used experimentally to generate spin polarization in semiconductors can be divided into the following four categories. The first type is optical excitation (optical spin orientation), which applies the optical selection rules in zinc-blend type semiconductors to produce the carrier-spin polarization [4, 56–58]. The second category uses electrical method to inject spin-polarized current from ferromagnetic materials into semiconductors [59–64]. The third type is to excite/inject spin-polarized current in a material such as metal or semiconductor through a time-dependent electric or magnetic field. In this method, a typical example is spin pumping [65–68]. The fourth category utilizes mutual conversion of current and spin-polarized current. In this method, the spin Hall effect or its inverse effect [69–71] is the most representative. Below, I introduce typical examples and relating principles for the optical orientation method.

Taking the zinc-blende III-V compound semiconductor material such as GaAs, I explain the optical orientation method [72]. The energy band structure of a bulk GaAs has a direct bandgap, and therefore the lowest energy point of the conduction band and the highest one of the valence band is located at the same  $\Gamma$  point, as shown in Fig. 1.7 (a). The conduction band (C. B.), neglecting its small spin-orbit coupling, is spin-degenerate. In the valence band (V. B.), it includes the degenerated light-hole (LH) and heavy hole (HH) bands. At  $k = 0$ , the energy difference between the C. B. and V. B. is expressed by a band-gap energy  $E_g$ . In GaAs, band-gap energy  $E_g$  is 1.43 eV at room temperature.

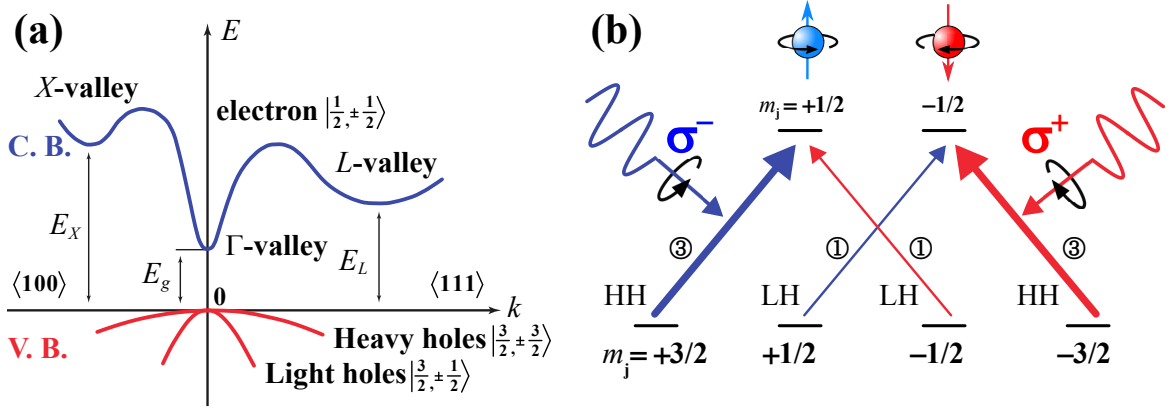


Figure 1.7: (a) Schematic band structure near the  $\Gamma$  point in GaAs. The energetical minimum of the C. B. and the maximum of the V. B. are located at  $k = 0$ . (b) Schematic diagram of the optical selection rule for inter-band transitions in a GaAs bulk with degenerate HH and LH bands and the corresponding optical polarization.

Considering that the projection of the photon angular momentum of circularly polarized light in its propagation direction is  $+1$  (right-handed polarization:  $\sigma^+$ ) or  $-1$  (left-handed one:  $\sigma^-$ ). When circularly polarized light can be absorbed in a semiconductor, the angular momentum of the light is transferred to the electron system, which can polarize carrier spins.

The probability of optical transitions ( $W_{if}$ ) can be calculated using the perturbation theory, which is generally written as the product of the transition matrix

elements  $M_{if}$  and the density of final states  $g(h\nu)$ . For the transition between bands, the transition probability is given by the Fermi's golden rule:

$$W_{if} = \frac{2\pi}{\hbar} M_{if} g(h\nu) = \frac{2\pi}{\hbar} \sum_{f,i} |\langle f | H_I | i \rangle|^2 (\delta E_f - E_i + \hbar\omega), \quad (1.8)$$

where  $i, f$  indicate the initial and final states of the optical transition with the energy of  $E_i$  and  $E_f$ , respectively.  $H_I$  is the interaction Hamiltonian.  $|J, m_j\rangle$  is the Bloch states according to the total angular momentum  $J$  and its projection onto a positive  $z$ -axis  $m_j$ . Wavefunctions describing C. B. and V. B. states close to the  $\Gamma$  point in terms of  $s, p_x, p_y$  and  $p_z$  orbital character are shown in Table 1.1.

Table 1.1: Specification of the C. B. and V. B. states close to the  $\Gamma$  point in a bulk GaAs [42, 72].

Band	$ J, m_j\rangle$	Wavefunction with spin states ( $\uparrow\downarrow$ )
Conduction	$ \frac{1}{2}, +\frac{1}{2}\rangle$	$ s\rangle \uparrow$
	$ \frac{1}{2}, -\frac{1}{2}\rangle$	$ s\rangle \downarrow$
Heavy hole (HH)	$ \frac{3}{2}, +\frac{3}{2}\rangle$	$-\frac{1}{\sqrt{2}}( p_x\rangle + i p_y\rangle) \uparrow$
	$ \frac{3}{2}, -\frac{3}{2}\rangle$	$+\frac{1}{\sqrt{2}}( p_x\rangle - i p_y\rangle) \downarrow$
Light hole (LH)	$ \frac{3}{2}, +\frac{1}{2}\rangle$	$-\frac{1}{\sqrt{6}}( p_x\rangle + i p_y\rangle) \downarrow -2 p_z\rangle \uparrow$
	$ \frac{3}{2}, -\frac{1}{2}\rangle$	$+\frac{1}{\sqrt{6}}( p_x\rangle - i p_y\rangle) \uparrow -2 p_z\rangle \downarrow$

The interaction Hamiltonian is an operator for physical interaction and given by:

$$H_I = \vec{\mu} \cdot \vec{\varepsilon} = (\mu_x \varepsilon_x + \mu_y \varepsilon_y + \mu_z \varepsilon_z), \quad (1.9)$$

where  $\vec{\mu}$  is the dipole moment of an electron and  $\vec{\varepsilon}$  is the electric field of an electromagnetic wave.

The Wigner–Eckart theorem indicates that only  $\Delta m_j = \pm 1$  are allowed for those non-zero matrix elements ( $M_{if} \neq 0$ ). Optical transitions in which  $m_j$  changes by  $\pm 1$ , reflecting the absorption of the photon’s original angular momentum. Holub et al summarized the relative transition probabilities by the square of the matrix element ( $M_{if}^2$ ) in Table 1.2 [42]. These selection rules are strictly valid at the  $\Gamma$  point only.

Table 1.2: Transition probabilities for allowed optical transitions with circular polarizations [42].

Transition states	$M_{if}$	$\Delta m_j$	Absorption light polarization	$ M_{if} ^2$
HH $\uparrow$ $\rightarrow$ CB $\uparrow$	$\langle \frac{1}{2}, +\frac{1}{2}   \mu_x   \frac{3}{2}, +\frac{3}{2} \rangle$	-1	$\sigma^-$	$\frac{1}{2}  \langle p_x   \mu_x   s \rangle ^2$
LH $\uparrow$ $\rightarrow$ CB $\downarrow$	$\langle \frac{1}{2}, -\frac{1}{2}   \mu_x   \frac{3}{2}, +\frac{1}{2} \rangle$	-1	$\sigma^-$	$\frac{1}{6}  \langle p_x   \mu_x   s \rangle ^2$
LH $\downarrow$ $\rightarrow$ CB $\uparrow$	$\langle \frac{1}{2}, +\frac{1}{2}   \mu_x   \frac{3}{2}, -\frac{1}{2} \rangle$	+1	$\sigma^+$	$\frac{1}{6}  \langle p_x   \mu_x   s \rangle ^2$
HH $\downarrow$ $\rightarrow$ CB $\downarrow$	$\langle \frac{1}{2}, -\frac{1}{2}   \mu_x   \frac{3}{2}, -\frac{3}{2} \rangle$	+1	$\sigma^+$	$\frac{1}{2}  \langle p_x   \mu_x   s \rangle ^2$

I use the absorption of  $\sigma^-$  polarized light propagating in the  $+z$ -direction as an example to explain the excitation process of spin polarization in the GaAs [42]. When the  $\sigma^-$  polarized light is absorbed with the excitation energy near  $E_g$ , electrons with the  $m_j = +3/2$  state in the HH band can show transition to the C. B. with  $m_j = +1/2$  state. At the same time, the electron transition between the  $m_j = +1/2$  in the LH band and the C. B. with  $m_j = -1/2$  can also take place. However, the excitation probabilities of such two processes are different. The transition probability of involving an LH or HH state is weighted by a square of the non-zero matrix element ( $M_{if}^2$ ) so that the relative intensity of the optical transition between the HH and LH subbands by circularly polarized light illumination is 3, as shown in Fig. 1.7 (b) [42] and in Table 1.2. Therefore, the absorption of photons with angular momentum  $-1$  ( $\sigma^-$  polarized light) produces three spin-up ( $m_j = +1/2$ ) and one spin-down ( $m_j = -1/2$ ) electrons. Therefore,  $\sigma^-$  polarized light creates 50% electron spin

polarization  $P$  in a bulk GaAs with the LH and HH subband degeneration at the  $\Gamma$  point, which is calculated as follows:

$$P = \frac{n_{\uparrow} - n_{\downarrow}}{n_{\uparrow} + n_{\downarrow}} = \frac{3 - 1}{3 + 1} = 50\%, \quad (1.10)$$

where  $n_{\downarrow}$  and  $n_{\uparrow}$  are the number of the optically excited electron with a spin  $m_j = -\frac{1}{2}$  and spin  $+\frac{1}{2}$ , respectively. However, when HH-LH splitting is sufficiently large,  $P \cong 100\%$ .

## 1.4 Spin polarization detection by light

Photoluminescence (PL) widely used in direct band-gap III-V compound semiconductors such as GaAs and InGaAs is a conventional optical method for detecting a spin polarization [4, 56]. Spin-polarized electrons can be optically excited from a V. B. to C. B. by illuminating circularly polarized lights, according to the abovementioned optical selection rule. Since the excited electron has a certain lifetime  $\tau$  after photo-excitation on the C. B., it will recombine with a hole on the V. B. emitting a circularly polarized light, depending on the degree of spin relaxation. When one assumes that the excited polarization is left-handed  $\sigma^-$ , the degree of the circular polarization (CPD) of PL is defined as:

$$\text{CPD} = \frac{I_{\sigma^-} - I_{\sigma^+}}{I_{\sigma^-} + I_{\sigma^+}}. \quad (1.11)$$

$I_{\sigma^-}$  and  $I_{\sigma^+}$  are co-circularly and cross-circularly polarized PL intensities against for the excitation light polarization.

It is known in Section 1.3 that the maximum CPD value with a bulk GaAs will be limited to 50% even though a carrier's spin polarization of 100%, obeying to the optical selection rule at the  $\Gamma$  point with LH and HH subband degeneration. However,

the case of QD is much more appealing as the quantum confinement and potential epitaxial strain lift the degeneracy between the HH and LH-band at the  $\Gamma$  point. For  $\text{In}_x\text{Ga}_{1-x}\text{As}$  QDs, those I used in my study using QW/QDs coupled structures, the HH-band is energetically higher (lower for a hole) than LH-band. Thus, the LH states can be ignored if all holes relax to the HH band before recombination with spin-polarized electrons, in addition to the  $\text{CB} \rightarrow \text{HH}$  transition is three times more probable than the  $\text{CB} \rightarrow \text{LH}$  transition. It is then theoretically possible to reach 100% CPD in PL emissions in the case that the injected electron-spin polarization is 100% [42]:

$$\text{CPD} = \frac{I_{\sigma^-} - I_{\sigma^+}}{I_{\sigma^-} + I_{\sigma^+}} \cong \frac{3n_{\uparrow} - 3n_{\downarrow}}{3n_{\uparrow} + 3n_{\downarrow}} = \frac{n_{\uparrow} - n_{\downarrow}}{n_{\uparrow} + n_{\downarrow}} = P. \quad (1.12)$$

# Chapter 2

## Research Purpose

### 2.1 Spin injection into QDs

Self-assembled quantum dots (QDs) of III-V compound semiconductors have been extensively investigated [73–75] owing to their unique and highly useful electronic properties, including significant suppression of carrier or exciton spin relaxation in addition to strong three-dimensional (3D) quantum confinements [4, 76–84]. Besides, these self-assembled QDs become an excellent candidate for the development of next-generation LED with a property of ultra-low energy consumption [85, 86].

For the practical use, high-density QDs are known to achieve efficient spin injection performance owing to suppression of Pauli spin blocking [87, 88], as well as high optical gains [79, 89–92]. Injection of spin-polarized carriers from the spin aligner into the active region is essential for realizing spin functional photoelectrical devices such as a spin-polarized LED [45, 47, 93]. Bulk semiconductors or QWs were used as active regions in the spin-LED [94]. However, the spin injection was not efficient because of the spin relaxation during the injection process in addition to the spin relaxation in the active region after the injection, particularly at high temperatures. Spin-relaxation times in these devices are in general very fast due to their 3D or 2D characters of

bulk or QW active regions, in addition to the 3D barriers [95]. However, in the QD-based spin-LED, the major spin-relaxation mechanism should be inactive [78,96–102]. Recently, QD-based spin-LEDs have been reported, which utilize QD-based active layers typically as shown in Fig. 2.1 [95,103–105]. Large magnetic fields ( $B > 2$  T) were used to align the magnetization perpendicular to a Fe film plane of a spin aligner (the saturation perpendicular magnetization was obtained at  $B > 2$  T with the strong in-plane magnetic anisotropy in the thin Fe film) to realize the Faraday geometry. An injection spin polarization of 5% in QDs was measured [103].

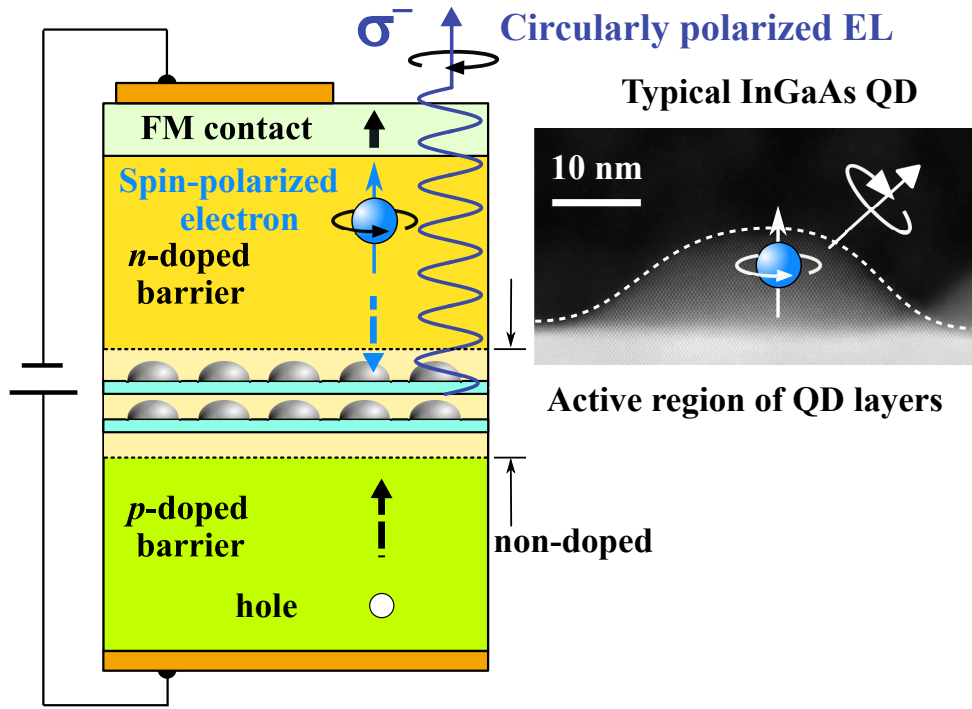


Figure 2.1: Schematic drawing of a QD-based spin-polarized LED structure with self-assembled InGaAs QDs in the active region. A typical cross-sectional TEM image of InGaAs QD is shown in right.

The spin-polarized electrons are injected into the QD-based active region and then circularly polarized lights can be emitted by recombination with un-polarized holes owing to the optical selection rule.

## 2.2 Spin injection in QW/QDs coupled nanostructures

Improving the spin injection efficiency into the QD-based spin-LED is a subject of intense research. Therefore, a spin injection process with the spatial transfer from a QW into QDs has introduced to improve the spin-injection efficiency. For this purpose, a QW/QDs tunnel-coupled nanostructure was proposed [106–110]. In this QW/QDs coupled nanostructure, a QD layer was coupled with an adjoining QW through a thin tunneling barrier (figure 2.2).

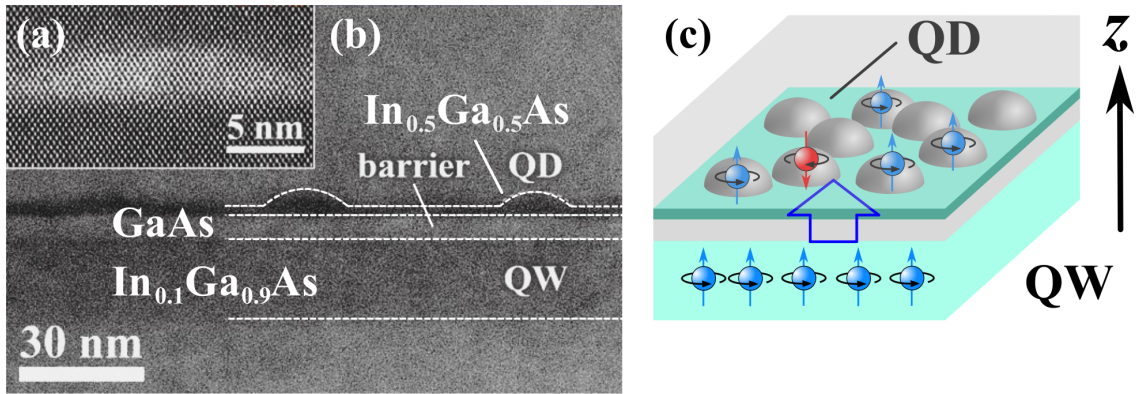


Figure 2.2: (a) Cross-sectional HAADF-STEM lattice image of QD in the QW/QD coupled nanostructure, where the degree of brightness indicates the In concentration. (b) Cross-sectional TEM image of the QW/QD coupled nanostructure with a 6-nm-thick GaAs barrier and 20-nm-thick In<sub>0.1</sub>Ga<sub>0.9</sub>As QW. (c) Schematic drawing of the QW/QD coupled nanostructure [110].

This tunnel-coupled QW/QDs nanostructure is expected to efficiently capture electron spins prior to spin relaxation, while electrons with lighter effective masses can be usually injected into QDs by Auger scattering or using electron blocking layers in layered device structures [111]. Our previous studies of QW/QDs nanostructures revealed an efficient and ultrafast spin injection with injection time constants ranging from 5 to 20 ps that maintain high degrees of spin polarization ( $> 90\%$ ) during tunneling from the QW to QD. Coupled states and the resultant spin injection from the 2D QW into 0D QDs are of interest due to the spin-conserving tunneling nature between

these different dimensionalities [110–113]. With increasing temperature up to 200 K, this spin-transfer dynamics was not affected; thus, the QW/QDs coupled nanostructures will promote the development of room-temperature device operation [110,114].

Figure 2.2 (a) shows a high-angle annular-dark-field (HAADF) scanning transmission electron microscopy (STEM) image of a cross-sectional QD structure in the QW/QDs coupled nanostructures. The thickness of barrier and QW are 6 nm and 20 nm, respectively. The typical QD diameter and height are 20 nm and 4 nm, respectively. Figure 2.2 (b) shows a cross-sectional TEM image of the layered QW/QDs coupled nanostructure, where clear interface among the QD layer, barrier, and QW are seen. Figure 2.2 (c) shows a schematic drawing of the QW/QD coupled nanostructure.

As shown in Fig. 2.3, the optical spin injection from the 2D-QW in to 0D-QDs shows three advantages in this subject [111]: First, more than 50% initial spin polarization of excitons can be generated in the QW; Second, spin injection from the QW into QDs via barrier can be ultrafast when the barrier is sufficiently thin; Last, the spin relaxation can be suppressed due to strong 3D quantum confinements in the QDs after the injection.

To apply this interesting QW/QDs coupled nanostructure to spin functional optical devices, effects of electric field on the spin dynamics should be investigated in detail. The tunnel-coupled QD-QW potentials can be precisely tuned by applying external electric fields along the growth direction. Therefore, the tunneling spin injection dynamics can be controlled by the electric field. Electric field control of the spin injection dynamics and the resultant spin states in high-density QDs will provide an effective approach exploring efficient spin injection through highly spin conserving resonant spin tunneling, which is potentially applied to semiconductor spintronics such as spin-polarized optical devices. Besides, we have observed both positive and negative trion formations with opposite electron spin directions in the QD ground

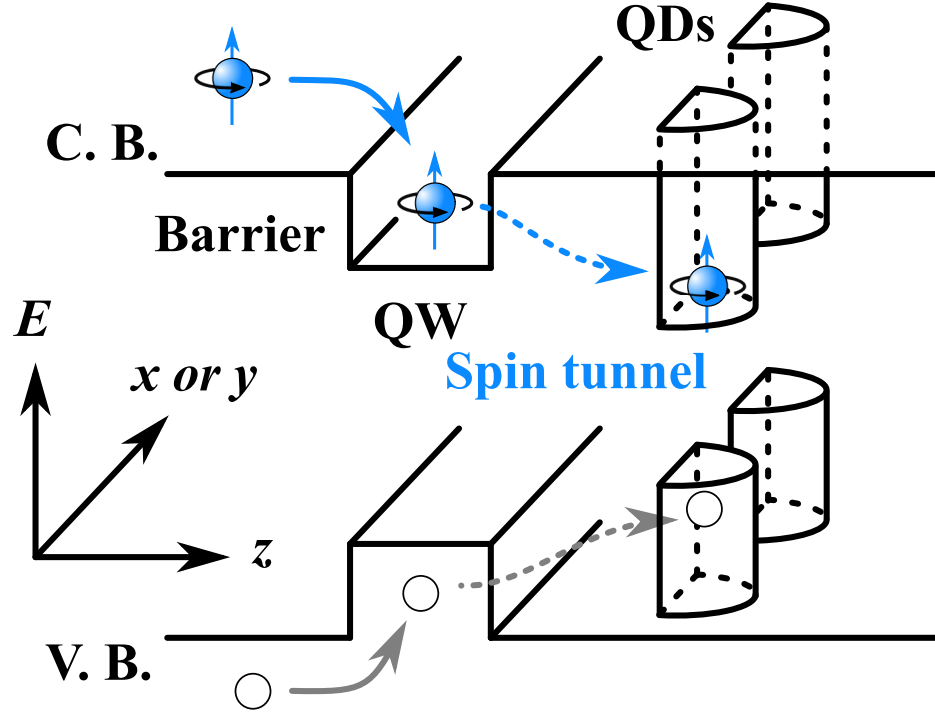


Figure 2.3: Schematic drawing of the band-structure and possible capture process of electron spins in the QW/QD coupled nanostructure.

states. This negative trion formation can significantly suppress the degree of circular polarization as a result of those spectra overlapping with opposite circular polarizations depending on the spin directions [115]. Therefore, the selective formation of positive and negative trions utilizing electric-field applications is also of great interest. This has a potential to enhance injected spin polarizations where the ratio of the number of electron and hole injections from a QW-based spin reservoir can be controlled by an electric field modification of the coupled QD-QW potential.

# Chapter 3

## Experimental Procedures

### 3.1 Layered QD-based sample and device structures

In this study, optical active layers composed of coupled QW/QDs coupled nanostructures of InGaAs were grown by molecular beam epitaxy. Figure 3.1 (a) shows a sample structure with the coupled QD-QW optical active layer. Non-doped GaAs layers with a 100-nm-thick  $\text{Al}_{0.1}\text{Ga}_{0.9}\text{As}$  barrier were grown at  $580^\circ\text{C}$  on a  $p$ -doped GaAs (001) substrate. An  $\text{In}_{0.1}\text{Ga}_{0.9}\text{As}$  QW with a thickness of 20 nm and a GaAs tunneling barrier with a thickness of  $d_B$  were then grown at  $520^\circ\text{C}$ . The substrate temperature was subsequently decreased to  $500^\circ\text{C}$  and a self-assembled  $\text{In}_{0.5}\text{Ga}_{0.5}\text{As}$  QD layer was grown. This QD layer was capped with a 10-nm-thick GaAs. Besides, a  $p$ -doped QD sample was prepared with Be in this capping layer, which will be described later. These QD-QW optical active layers were covered at  $580^\circ\text{C}$  by a top 60-nm-thick  $\text{Al}_{0.2}\text{Ga}_{0.8}\text{As}$  barrier capped with a 10-nm-thick GaAs. The top and bottom AlGaAs barriers ensure that carriers are condensed in proximity to the QD-QW active layer, in addition to suppressing a current flow. A Ti/Au electrode was deposited on the top of this semiconductor layered structure and a  $10\text{-}\mu\text{m}$ -square

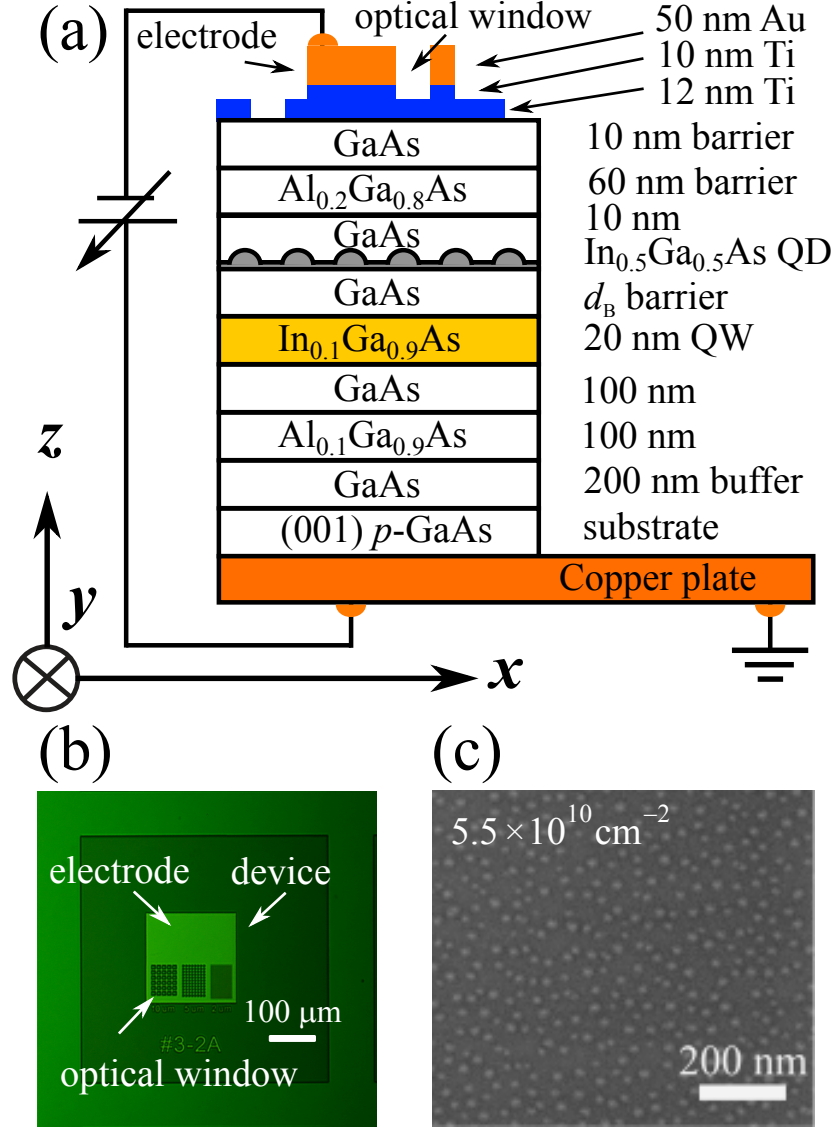


Figure 3.1: (a) Schematic drawing of the electric-field-effect optical device structure with an optically active layer of the non-doped QW/QDs coupled nanostructure. (b) Optical image of the surface of the device structure. (c) SEM image of the QD surface of the reference sample with identical growth conditions.

optical window was fabricated enabling optical spin excitations and PL observations, as shown in Fig. 3.1 (b). The average base diameter and height of the QDs were 20 and 5 nm, respectively, with a high areal density of  $5.5 \times 10^{10} \text{ cm}^{-2}$  as shown in Fig. 3.1 (c).

Figure 3.2 (a) shows a schematic drawing of the concept device using an optically active layer of the coupled QW/QDs nanostructure. The coupled potentials as a

function of the electric field were calculated by the NEXTNANO simulator [116,117]. Spin-polarized carriers were initially excited in the QW selectively by irradiating circularly polarized lights with a specific energy slightly above the QW bandgap. Subsequently, the injected spin states via tunneling can be detected as a function of electric field by observing circularly polarized PL from the QDs, which obeys the optical selection rule [58], as shown in Fig. 3.2 (b). The effect of  $p$ -doping in the QDs was also examined to investigate trion formation in the spin injection process.

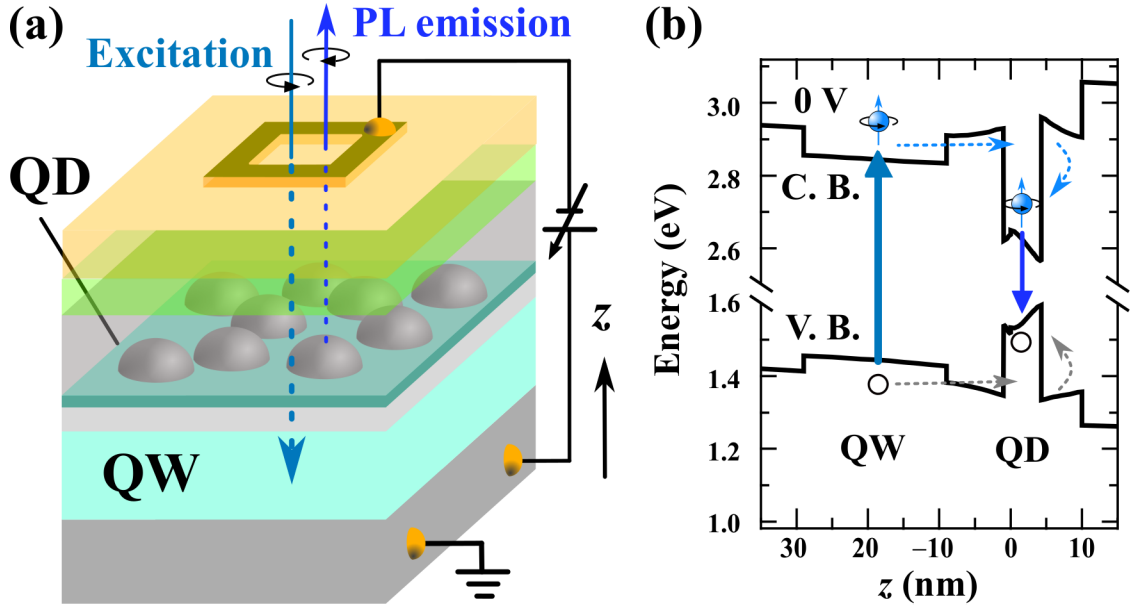


Figure 3.2: (a) A schematic drawing of optical spin generation and detection in the non-doped coupled nanostructure controlled by an electric field. (b) An example of the 3D-calculated potential of the C. B. and V. B. with a barrier thickness of  $d_B = 8$  nm at a bias voltage of 0 V along the growth direction ( $z$ -axis) of the coupled In-GaAs QW/QDs nanostructure grown on a  $p$ -doped GaAs substrate and the resultant electron-spin injection process.

## 3.2 Optical measurement

Figure 3.3 (a) shows a conventional micro-PL ( $\mu$ -PL) measurement setup used in this study [118]. The samples were set at 4 K on a cold-finger of the cryostat. The excitation was made using  $\sigma^-$  circularly polarized lights selectively for the QW at

1.459 eV. This energy was above the QW bandgap while sufficiently below a GaAs-barrier bandgap of 1.519 eV, as shown in Fig. 3.3 (b). A mode-locked Ti:Sapphire pulsed laser with a repetition rate of 80 MHz and a temporal width of 150 fs was also used as the excitation source for time-resolved  $\mu$ -PL measurements. The CPD of excited electrons in the QW is expected to be 50–100% depending on the degree of hole mixing with the optical selection rule, where heavy and light holes can be excited by the above femtosecond laser with a relatively broad spectral width of 22 meV, as shown in Fig. 3.3 (b).

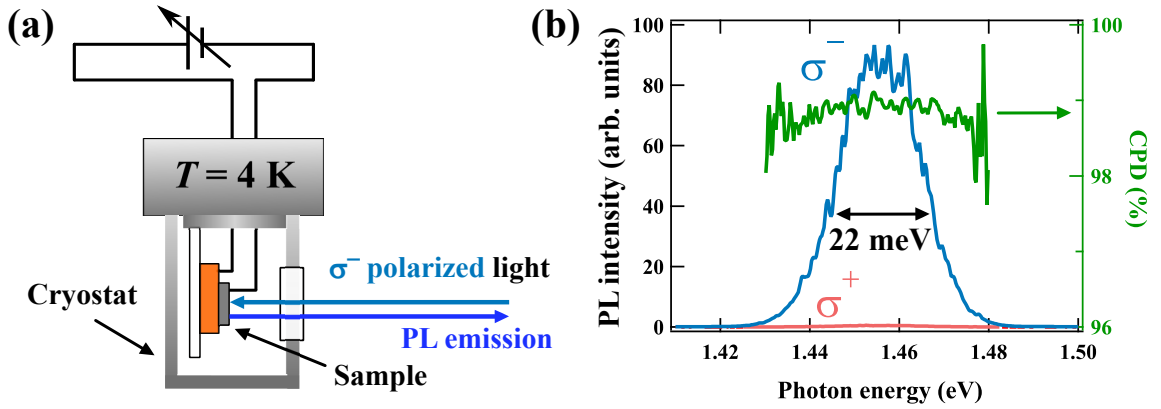


Figure 3.3: (a) Schematic drawing of a  $\mu$ -PL setup. (b) The excitation laser spectra with  $\sigma^-$  circularly polarization with the degree of circular polarization (CPD) of 99%.

A focused laser beam is irradiated on the sample surface, which was set onto a cold-finger of a liquid-He flow type cryostat. The QD-PL emission from the sample was collected through an objective lens ( $\times 20$ ) with a numerical aperture of 0.35. A combination of circular polarization filter with a linear polarization one and some pass filters were used for the detection of circular polarization property of PL. The sample surface in the device was observed using a conventional charged-coupled device (CCD) camera. In order to measure the  $\mu$ -PL spectra, the QD-PL emission is corrected and introduced to a monochromator using a bundled optical fiber and then detected by a highly sensitive CCD cooled by liquid-nitrogen. An external bias along the growth

direction [ $z$ -direction in Fig. 3.2 (a)] of the semiconductor layers was applied, ranging between  $-3$  and  $+3$  V.

Time-resolved PL (TRPL) [119–121] was also measured at 4 K by using time-correlated single-photon counting (TCSPC) with a time resolution of 40 ps.

Additionally, I-V curves were measured after device fabrication under room temperature. Figure 3.4 shows a typical I-V characteristic curve. For the bias voltage increase from  $-5.0$  to  $+5.0$  V, the leak current through the device was sufficiently suppressed less than 2 mA. I measured optical properties in the devices under bias application ranging from  $-3$  to  $+3$  V without a significant leak current.

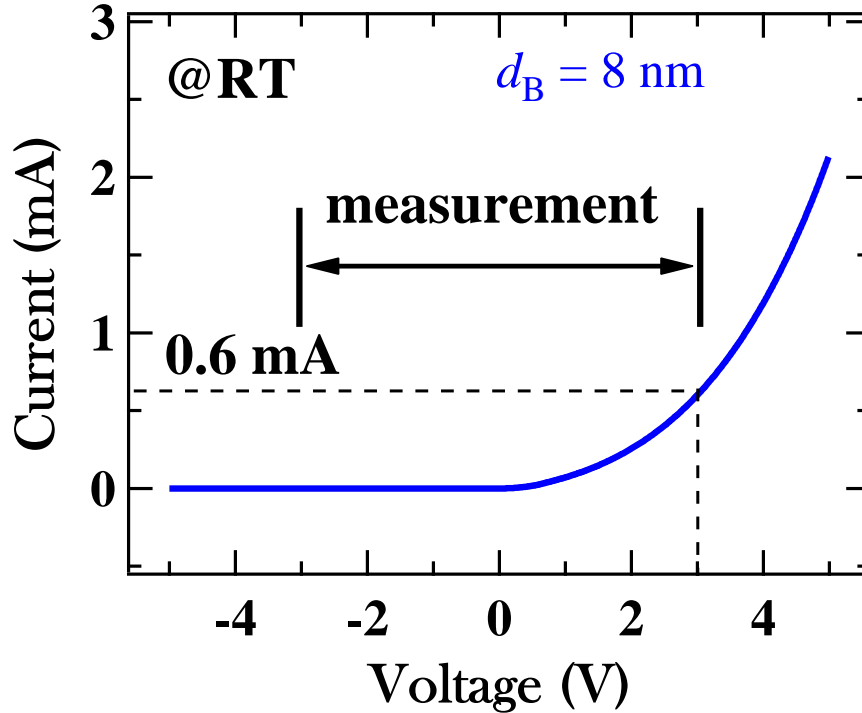


Figure 3.4: A typical I-V curve of the device with a GaAs tunneling barrier thickness of 8 nm.

# Chapter 4

## Efficient electron-spin injection into QD by electric field application

### 4.1 Excitation light power dependence

#### 4.1.1 QD-PL behavior

Here, I measured PL spectra from the QDs as a function of bias voltage. Figure 4.1 (a) shows a typical contour plot of the QD-PL intensity as functions of photon energy and bias voltage, in a device sample with a QW/QDs coupled active layer without *p*-doping and with a tunneling barrier thickness ( $d_B$ ) of 8 nm. The PL energies exhibiting intense PL, ranging from 1.24 to 1.32 eV, correspond to the QD ground states (GSs) of the QD ensemble. Above 1.32 eV, the PL from the excited states (ESs) is observed; however, its intensity is rather weak under this relatively low excitation power.

Figures 4.1 (b)-(d) show calculated potentials around the QW/QDs coupled nanostructure along the growth direction with external biases of  $-1.5$  V,  $0.5$  V, and

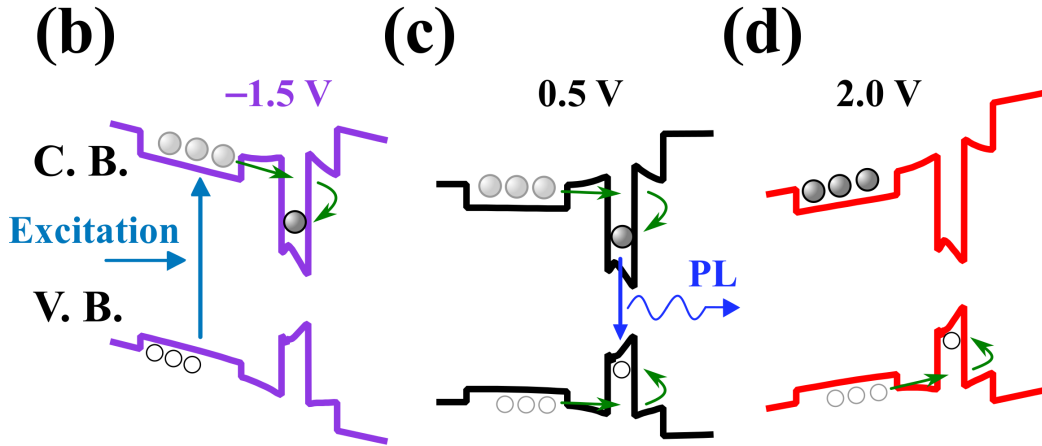
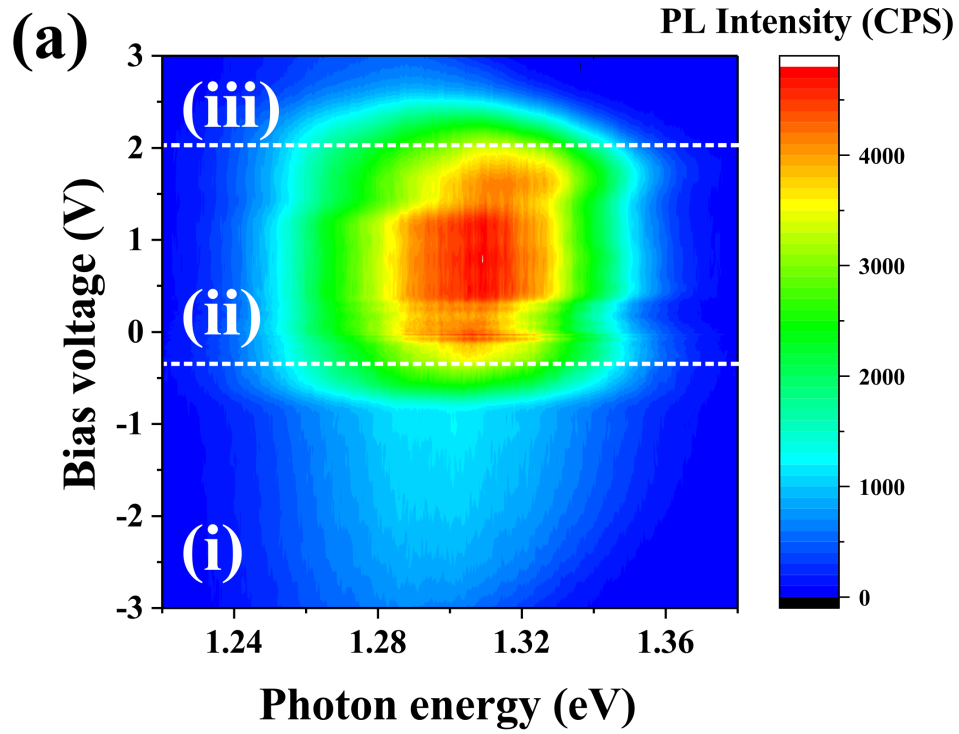


Figure 4.1: (a) A contour plot of PL intensity at 4 K from un-doped QDs with  $d_B = 8$  nm as functions of photon energy and bias voltage under an excitation laser power of  $320 \mu\text{W}$ . 3D-calculated potentials of the C. B. and V. B. as a function of growth direction ( $z$ -axis) in the coupled QW/QDs nanostructure with bias voltages of  $-1.5$  V (b),  $0.5$  V (c), and  $2.0$  V (d). The carrier dynamics after photo-excitation in the QW are schematically illustrated.

+2.0 V, respectively. As shown in Fig. 4.1 (a), the contour plot of un-doped QD-PL intensity can be divided into 3 areas: (i), (ii), and (iii), as shown in the figure. These three bias areas are characterized as follows: (i) The PL intensity decreases with increasing negative bias toward  $-2.0$  V. This result can be attributed to hole localization opposite from the QD side in the QW, as shown in Fig. 4.1 (b). This localization of hole in the QW apart from the QD side weakens the QD-PL intensity. (ii) The PL intensity increases significantly above 0 V and shows a maximum around 1 V, indicating efficient carrier injection from the QW into the QDs by tunneling, as shown in Fig. 4.1 (c). (iii) Above 1 V, the PL intensity decreases again, where electrons can be likely confined to one side of QW opposite from the neighboring QD layer, as shown in Fig. 4.1(d). These changes can be caused by electric-field-induced band bending.

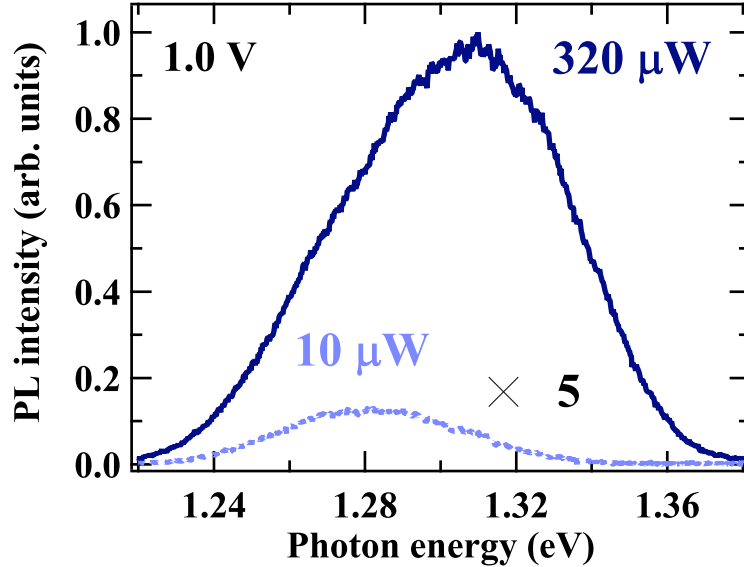


Figure 4.2: QD-PL spectra with 1.0 V under excitation powers of  $320 \mu\text{W}$  (a dark blue solid line) and  $10 \mu\text{W}$  (a light blue dotted line) in the sample with  $d_B = 8$  nm.

The QD-PL spectrum with an excitation power of  $320 \mu\text{W}$  at the bias voltage of 1.0 V is shown in Fig. 4.2, compared to that with a sufficiently lower excitation power of  $10 \mu\text{W}$  (a light blue dotted line). The QD-PL spectrum with the latter  $10 \mu\text{W}$  excitation indicates the inhomogeneous GS distribution in this high-density

QD ensemble sample. The peak energy of the QD-PL spectrum with an excitation power of  $320 \mu\text{W}$  shifts to the higher-energy side due to a state filling effect [122] in this QD ensemble.

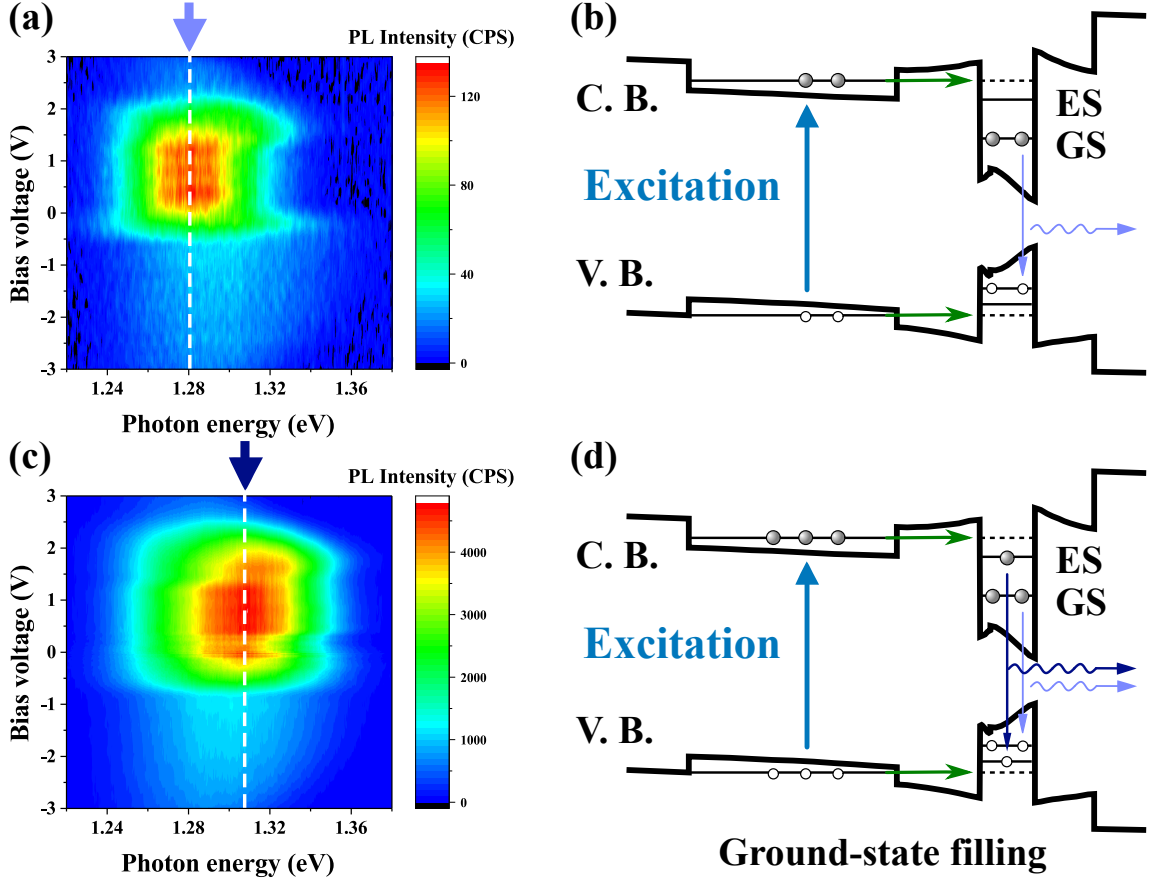


Figure 4.3: Contour plots of the QD-PL intensity with  $d_B = 8 \text{ nm}$  as a function of excitation power: (a)  $P_{exc} = 10 \mu\text{W}$  and (b) the corresponding schematic carrier states, (c)  $P_{exc} = 320 \mu\text{W}$  and (d) the schematic illustration of the state filling effect at the QD-GS in the latter case of higher  $P_{exc} = 320 \mu\text{W}$ .

Figure 4.3 (a) and (c) show contour plots of the QD-PL intensity for the above two cases. High PL intensities are observed, ranging from  $-0.5 \text{ V}$  to  $+2.0 \text{ V}$  independent of the excitation power ( $P_{exc}$ ) owing to the electron or hole depletion. GS-PL is dominant with energy less than  $1.32 \text{ eV}$  [Fig. 4.3 (b)], which was known from the PL spectrum at the low excitation power of  $10 \mu\text{W}$  in Fig. 4.2. PL intensities from QD-ESs above  $1.32 \text{ eV}$  become stronger than those of the GSs and more dominant with

increasing power. Figure 4.3 (d) explains this situation of GS-state filling with higher  $P_{exc} = 320 \mu\text{W}$ .

#### 4.1.2 Circularly polarized QD-PL spectra

Figure 4.4 shows circularly polarized PL spectra for the un-doped QD sample with  $d_B = 8 \text{ nm}$ , under an excitation power of  $320 \mu\text{W}$  and a bias voltage of  $1.0 \text{ V}$ . A QD-PL spectrum at a sufficiently lower excitation power of  $10 \mu\text{W}$  is also shown by a black dotted line. A co-circular ( $\sigma^-$ ) spectrum for the excitation polarization is plotted using a blue line, while cross-circular ( $\sigma^+$ ) one is shown by a red line.

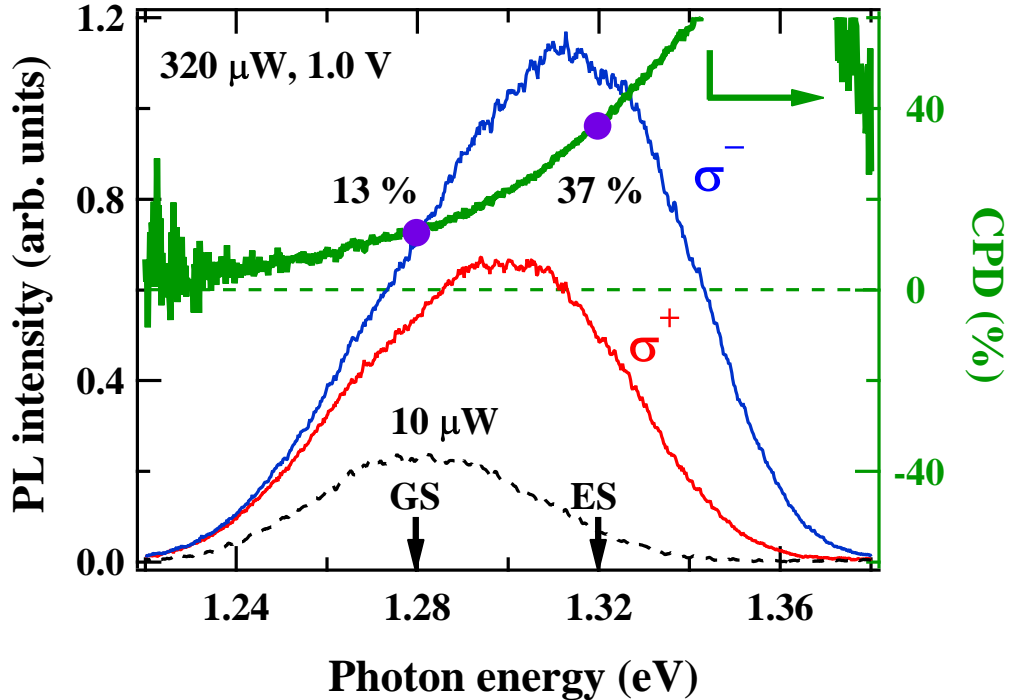


Figure 4.4: Circularly polarized PL spectra (co-circular  $\sigma^-$ ; a blue line, cross-circular  $\sigma^+$ ; a red line, and the corresponding CPD value; a green line) under  $\sigma^-$  excitation at  $4 \text{ K}$  with  $1.0 \text{ V}$  in the un-doped QD sample ( $d_B = 8 \text{ nm}$ ). A black dotted line indicates the un-polarized PL spectrum under an excitation power of  $10 \mu\text{W}$ . Purple closed-circle marks indicate CPD values corresponding to the GS and ES energy peaks in the QD-PL, respectively.

This circularly polarized PL was detected from the QDs after the carrier (spin) injection from the QW. The circular polarization degree (CPD) reflecting the electron spin polarization at emissive states is expressed by:

$$\text{CPD} = (I_{\sigma^-} - I_{\sigma^+}) / (I_{\sigma^-} + I_{\sigma^+}), \quad (4.1)$$

where  $I_{\sigma^\mp}$  is left- or right-handed ( $\sigma^\mp$ ) circularly polarized QD-PL intensities after  $\sigma^-$  excitation for the QW. The corresponding QD-CPD value obtained from the QD-PL spectra is also plotted as a function of photon energy, as a green line in Fig. 4.4.

A positive CPD property (co-circular; parallel spin to the initial QW spin) is dominant even at GSs with 1.0 V in Fig. 4.4. With an increase of photon energy, the value of CPD increases from 13% at GS (1.28 eV) up to 37% at ES (1.32 eV).

### 4.1.3 CPD value of QD-PL

Figure 4.5 shows contour plots of the CPD value in the un-doped QD-PL, under excitation powers of 10  $\mu\text{W}$  and 320  $\mu\text{W}$ . These contour plots of CPD are composed of a series of QD-CPD value as functions of photon energy and bias. The circularly polarized PL reflecting carrier spin states shows the following properties.

Positive CPD values ranging from 10% to 30% are observed above 0.2 V around the PL-intensity peak, indicating a parallel spin state to the initial spin direction in the QW. A higher energy side corresponding to the QD-ESs exhibits higher CPD values. These co-circular PL characteristics clearly show efficient spin injection from the 2D-QW to 0D-QDs in this coupled nanostructure [110,113,114]. As can be seen in Fig. 4.5 (b), high positive (CPD) values greater than 60%, indicating highly efficient injection, are observed ranging from 0 to 2.5 V under 320  $\mu\text{W}$ .

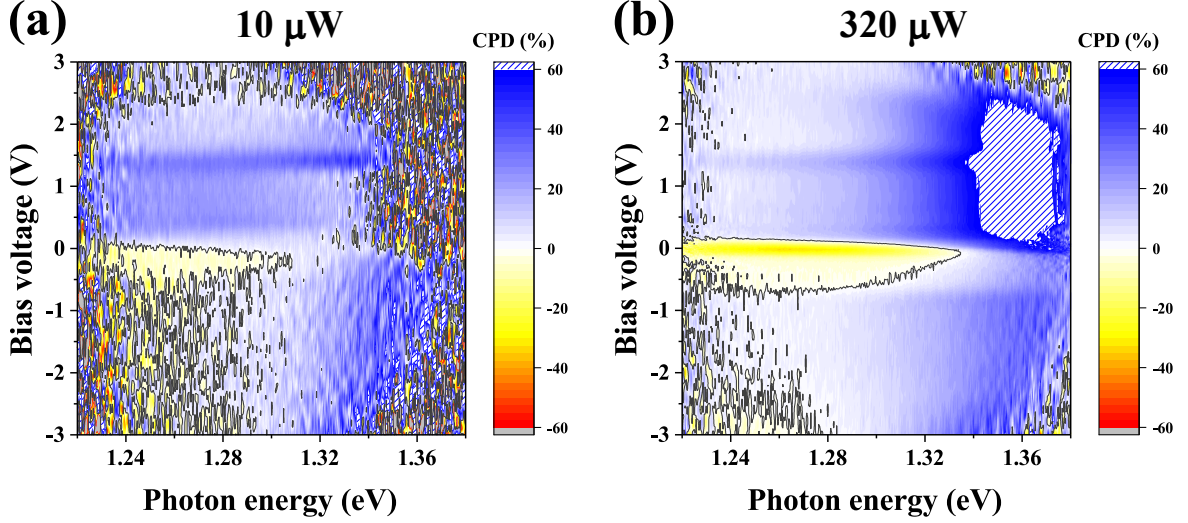


Figure 4.5: Contour plots of a CPD value at 4 K as functions of photon energy and bias voltage under excitation powers of  $10 \mu\text{W}$  (a) and  $320 \mu\text{W}$  (b), for the un-doped QD sample with  $d_B = 8 \text{ nm}$ .

In contrast, I find a clear bias region from  $-0.7$  to  $0.1 \text{ V}$  exhibiting negative CPD values in Fig. 4.5 (b). This phenomenon of negative CPD will be discussed in the next chapter.

#### 4.1.4 Circularly polarized time-resolved QD-PL

Circularly polarized transient PL and the corresponding CPD from the QD-GS as a function of excitation power are shown in Fig. 4.6, with the same bias voltage of  $1.0 \text{ V}$ . Marked initial positive polarization up to 30% appears at this  $1.0 \text{ V}$  for all powers. The CPD values decrease steeply within  $0.2 \text{ ns}$  for the high power case in Fig. 4.6 (c), while it decreases slowly longer than  $2 \text{ ns}$  for the lower power in Fig. 4.6 (a). The initial positive CPD can reflect an initial spin polarization just after tunneling from the QW, indicating the spin-injection efficiency.

In Fig. 4.6 (c), the positive polarization about 10% remains beyond  $0.2 \text{ ns}$ . This time persistent positive CPD suggests that the parallel spins are continuously injected from the QW after the tunneling [123]. The spin-relaxation time was about  $1 \text{ ns}$  in a single layer QD sample without the QW grown under identical conditions.

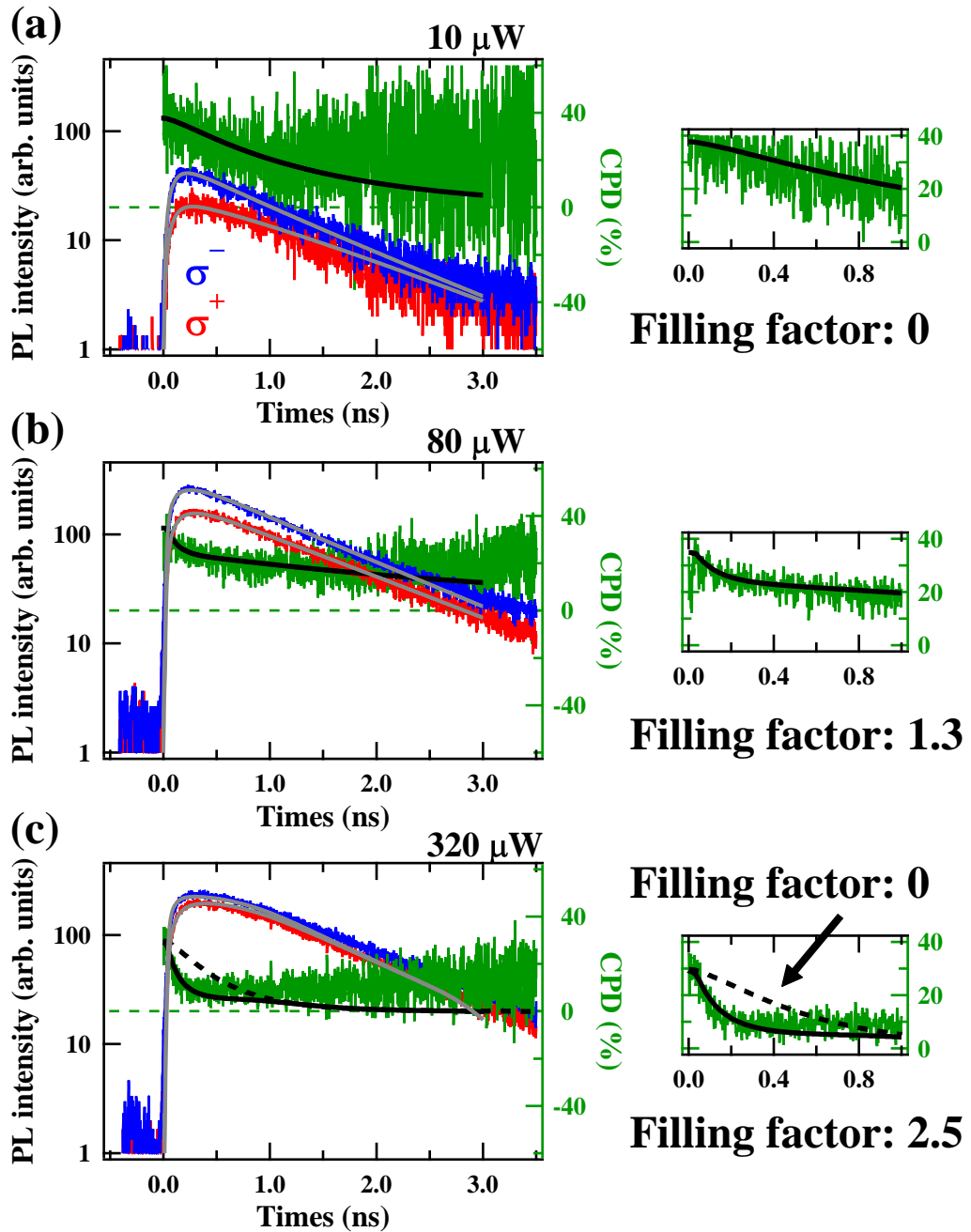


Figure 4.6: Circularly polarized time-resolved QD-PL (co-circular  $\sigma^-$ : a blue line, cross-circular  $\sigma^+$ : a red line, and the corresponding CPD value: a green line) for the GS with 1.0 V at 4 K, under the  $\sigma^-$  excitations of 10 (a), 80 (b), and 320  $\mu\text{W}$  (c). Rate-equation calculations are shown taking the state-filling effect at the GS into account (solid black lines). The time-dependent CPD calculated without this filling is also shown by a broken line for the (c).

An electron spin relaxation in the QW before the spin injection can be suppressed by hole separation from the electron within the QW owing to the band bending, where a dominant Bir-Aronov-Pikus spin relaxation mechanism in the QW at low temperatures becomes inactive [124, 125].

To analyze circularly polarized time-resolved QD-PL, I used a rate-equation model [87], given as follows:

$$\frac{dN_{QW}(t)}{dt} = -\eta \frac{D_s - N_2^{\sigma^-}(t)}{D_s} \frac{N_{QW}(t)}{\tau_{inj}} - (1 - \eta) \frac{D_s - N_2^{\sigma^+}(t)}{D_s} \frac{N_{QW}(t)}{\tau_{inj}}, \quad (4.2)$$

$$\frac{dN_2^{\sigma^-}(t)}{dt} = \eta \frac{D_s - N_2^{\sigma^-}(t)}{D_s} \frac{N_{QW}(t)}{\tau_{inj}} - \frac{N_2^{\sigma^-}(t)}{\tau_r} - \frac{N_2^{\sigma^-}(t)}{\tau_s} + \frac{N_2^{\sigma^+}(t)}{\tau_s}, \quad (4.3)$$

$$\frac{dN_2^{\sigma^+}(t)}{dt} = (1 - \eta) \frac{D_s - N_2^{\sigma^+}(t)}{D_s} \frac{N_{QW}(t)}{\tau_{inj}} - \frac{N_2^{\sigma^+}(t)}{\tau_r} - \frac{N_2^{\sigma^+}(t)}{\tau_s} + \frac{N_2^{\sigma^-}(t)}{\tau_s}. \quad (4.4)$$

The initial number of exciton in the QW is expressed by  $N_{QW}$  with the  $\sigma^-$ -polarization. Co-polarization excitons  $\eta N_{QW}(t)$  and cross-polarization excitons  $(1-\eta)N_{QW}(t)$  are injected into the GS of a QD, where spin conservation in the spin-injection process is expressed by a parameter of  $\eta$ .  $\tau_{inj}$  and  $\tau_r$  are a time constant of the exciton injection from the QW to the QD-GS and that of the relaxation from the GS state, respectively.  $\tau_s$  is a time constant of spin relaxation between these spin-polarized states in the QD-GS.  $N_2^{\sigma^\mp}(t)$  denote the numbers of spin-polarized exciton at the GSs with  $\sigma^\mp$ . The parameter  $\tau_r$  can be expressed as follows:

$$\frac{1}{\tau_r} = \frac{1}{\tau_{rad}} + \frac{1}{\tau_{nr}}, \quad (4.5)$$

where  $\tau_{rad}$  and  $\tau_{nr}$  are time constants of radiative and non-radiative decay processes.  $D_s$  is the density of the states at this GS in the QD. The factor  $f(t) \equiv \frac{N_{QW}(t)}{D_s}$  indicates the degree of time-resolved state filling due to the Pauli exclusion principle in the QD, against for the initial population in the QW, where larger  $f$  expresses more significant filling.

By using this rate-equation model [87,88,110,113,126], I can fit the time-resolved QD-PL as shown in Fig. 4.6 (a)-(c). Solid black lines show the best-fit calculations with the state filling factors of 0, 1.3, and 2.5, for (a)-(c), respectively. A significant state filling effect is observed under the highest excitation power, which is quite natural. As shown in Fig. 4.6 (c), the steep CPD decrease can be well explained by this QD-GS state filling effect (a solid line) compared to that without this filling (a broken black line) after the subsequent electron tunneling. By contrast, the states of the QDs are rarely occupied at low excitation powers. Thus, the state filling effect plays a little role [Fig. 4.6 (a)].

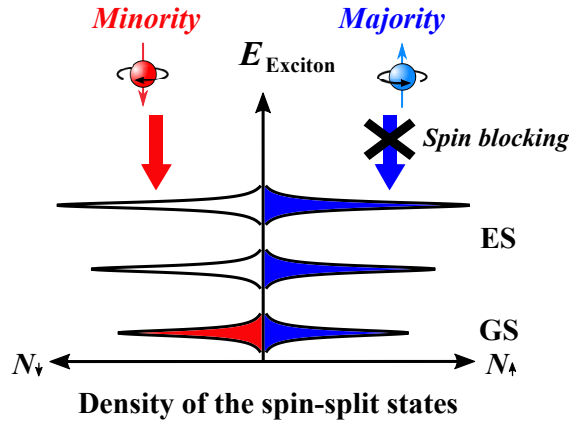


Figure 4.7: Schematic illustration of spin-dependent injection of electrons into the QD states, taking the spin-dependent state filling and the resultant spin blocking into account [88].

At the lowest excitation power of  $10 \mu\text{W}$ , the maximum CPD value at time  $t = 0$  indicates the initial CPD value in the QD after the spin injection. The subsequent decrease of CPD reflects spin relaxation inside the QD with a spin relaxation time ( $\tau_s$ ) of 2.9 ns. When the excitation power is sufficiently strong to induce the filling, the fast decay of the CPD less than 0.4 ns can be quantitatively explained by this spin-dependent filling in the QDs, as illustrated in Fig. 4.7 [87, 114]. The majority spin-up electrons generated by  $\sigma^-$ -polarized light pulses immediately occupies the same  $\sigma^-$ -polarized GS and ESs in the QDs after the spin injection, and additional

spin injection can be blocked by this spin-state filling. However, spin-down minority electrons can be injected into the GS in the QDs, continuously. Therefore, the CPD value at GS decreases rapidly because of the low density of the GS.

## 4.2 Effect of tunneling barrier thickness

Figures 4.8 (a)–(c) show contour plots of the QD–PL intensity with an excitation power of  $40 \mu\text{W}$ , for various tunneling barrier thicknesses ( $d_B$ ). PL from GSs of the QD ensemble is dominant with the emission energies less than  $1.32 \text{ eV}$ , which was known from the PL spectrum observed with the previous lowest excitation case of  $10 \mu\text{W}$ . The PL intensity decreases at a bias voltage of approximately  $+2 \text{ V}$ , independent of  $d_B$ . This can be observed by increasing the electron barrier height from the QW toward the QD, preventing electron injection into the QDs. The maximum PL intensity depends on  $d_B$ , where the intensity ratio becomes more systematic at high excitation powers; i.e., 4:3:2 at  $640 \mu\text{W}$  with  $d_B = 8 \text{ nm}$ ,  $10 \text{ nm}$ , and  $20 \text{ nm}$ , respectively. Electron wave-function calculations show that the tunneling probability can be suppressed to some extent with  $d_B = 20 \text{ nm}$  under flat band conditions.

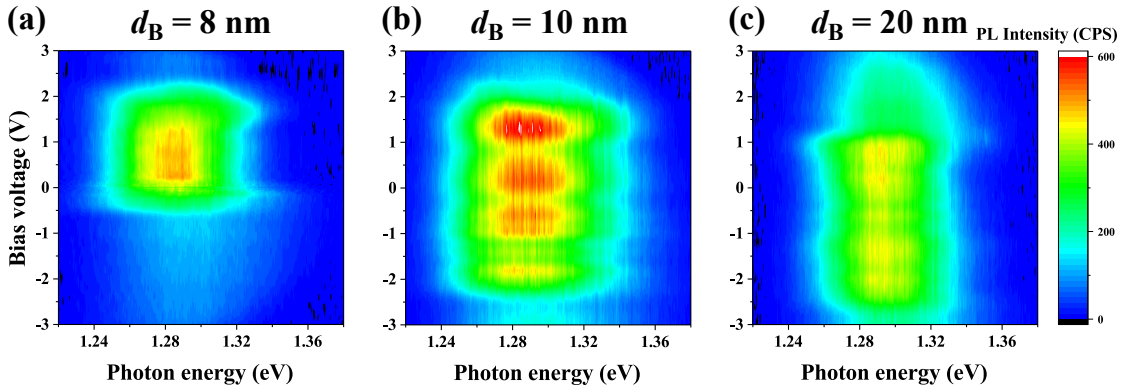


Figure 4.8: Contour plots of the QD–PL intensity as functions of photon energy and bias voltage at  $4 \text{ K}$  under an excitation power of  $40 \mu\text{W}$  in the QW/QDs samples with (a)  $d_B = 8 \text{ nm}$ , (b)  $d_B = 10 \text{ nm}$ , and (c)  $d_B = 20 \text{ nm}$ , respectively.

Direct carrier excitation inside the QDs seems to contribute the PL intensity obtained with  $d_B = 20$  nm; in contrast, the volume ratio of the single QD layer is less than 5% for the 20-nm-thick QW. Besides, one can also take into account the energy transfer of excitons due to an electric dipole-dipole interaction, where the transfer rate is known to be strongly dependent on the distance, such as  $d_B^{-4}$  [127, 128]. A theoretical model and experimental results in semiconductor quantum structures including localized exciton states showed the so-called photon exchange energy transfer, with the transfer rate rather slowly varying as a function of distance [123, 129]. The starting bias of the PL intensity decrease shifts toward the more negative bias side with increasing  $d_B$ . Hole injection starts to be inactive below 0 V, as shown in Fig. 4.1. (d), which agrees well with the case of  $d_B = 8$  nm in Fig. 4.8 (a). Therefore, the shift of the starting bias of PL decrease with larger  $d_B$  suggests that a hole escape from the QDs to the QW is responsible for the PL intensity decrease, where the thicker tunneling barrier reduces the hole-escape rate. An oscillation behavior of the PL intensity as a function of bias is clearly seen with  $d_B = 10$  nm in Fig. 4.8 (b). This oscillation is repeatable and is discussed later.

Next, we show the circular polarization property of the QD-PL as a function of  $d_B$  in Fig. 4.9 (a)-(c).

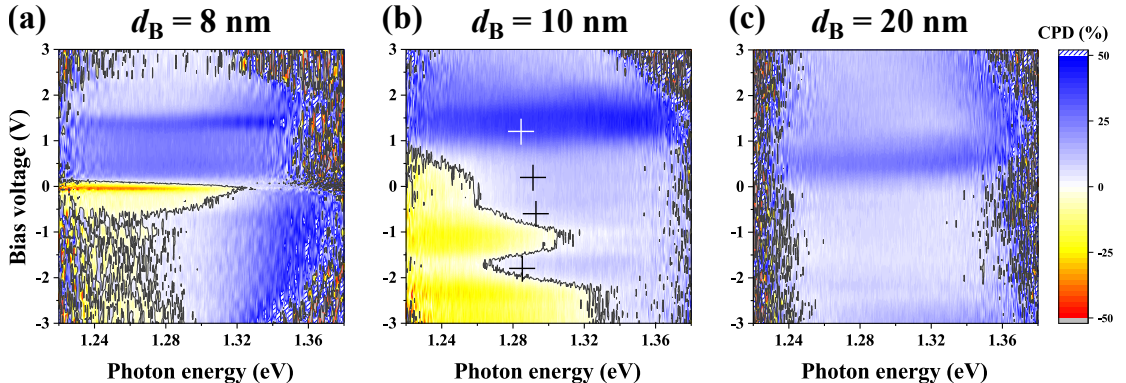


Figure 4.9: Contour plots of the CPD value of the QD-PL with (a)  $d_B = 8$  nm, (b)  $d_B = 10$  nm, and (c)  $d_B = 20$  nm. White and black crosses in (b) indicate the PL intensity peak position of the oscillation behavior, as shown in Fig. 4.8 (b).

As can be seen in Fig. 4.9 (b), high positive CPD values (co-circular polarization, thus the parallel spin state to the initial direction in the QW) greater than 40% (indicating highly efficient spin injection) are observed at a bias voltage of approximately +1.5 V with  $d_B = 10$  nm. The PL energies exhibiting intense PL, ranging from 1.24 to 1.32 eV, correspond to the QD-GSs. Above 1.32 eV, the PL from the ESs is observed; however, its intensity is rather weak at this relatively low excitation power. The sharp bias dependence of positive CPD is also seen at the ESs with  $d_B = 8$  nm. The background positive CPD of 20%–30% is seen for all samples with positive biases, indicating the usual spin-injection phenomenon. Negative CPD regions are also obtained at a bias voltage of less than 0 V (negative bias region), depending on  $d_B$ . This can be attributed to negative trion formation [130–135]; the detailed bias dependence is discussed later. A negative trion can be formed in QDs with excess electrons compared to the number of holes. Therefore, the appearance of this negative CPD region coincides well with the bias region corresponding to the excess electron injection or hole escape, which is known from the bias dependence of the PL intensity as discussed above. It is noted that the positive CPD value is enhanced (becomes more positive) or the negative CPD value is weakened around the biases, indicating stronger PL intensities, as shown by a cross in Fig. 4.9 (b). This suggests efficient parallel spin injection at specific bias applications, which is also discussed later.

## 4.3 Resonant tunneling and oscillation behaviors of the PL intensity

### 4.3.1 Resonant tunneling induced by wetting layer and LO-phonon emission

Excitation power dependence of the PL intensity and the CPD value in the QD–QW sample with  $d_B = 10$  nm are shown in Fig. 4.10. High PL intensities are observed, ranging from  $-2$  V to  $+2$  V for the whole powers. PL intensities from QD–ESs above 1.32 eV become stronger than those of the GSs and more dominant with increasing power as well as the previous  $d_B = 8$  nm sample. The intensity maximum increases with increasing power, where an oscillation of the intensity as a function of bias is observed at high powers, as shown in Fig. 4.10 (b) and (c), and is also discussed later.

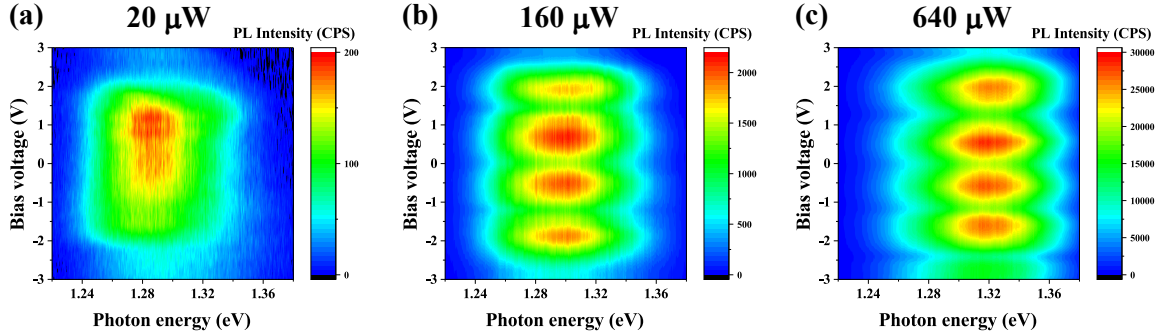


Figure 4.10: Contour plots of the QD–PL intensity with  $d_B = 10$  nm as a function of excitation power: (a)  $20 \mu\text{W}$ , (b)  $160 \mu\text{W}$ , and (c)  $640 \mu\text{W}$ , respectively.

The bias dependence of the CPD, as shown in Fig. 4.11, shows the following trends. Significantly high values of positive (parallel spin to the initial direction in the QW) CPD of 40% or higher is observed at  $+1.0\sim 1.6$  V in the GSs, as well as ESs with  $20 \mu\text{W}$ , as shown in Fig. 4.11 (a). This trend is also seen at  $+1.2\sim 2.2$  V in ESs with  $160 \mu\text{W}$ , as shown in Fig. 4.11 (b). The excitation power of  $40 \mu\text{W}$  shows an intermediate trend, as observed in Fig. 4.9 (b). The CPD values at GSs degrade at higher excitation powers, as shown in Fig. 4.11 (c) with  $640 \mu\text{W}$ . This

power dependence of spin injection degradation at the GSs can be explained by a spin state filling effect [87, 88].

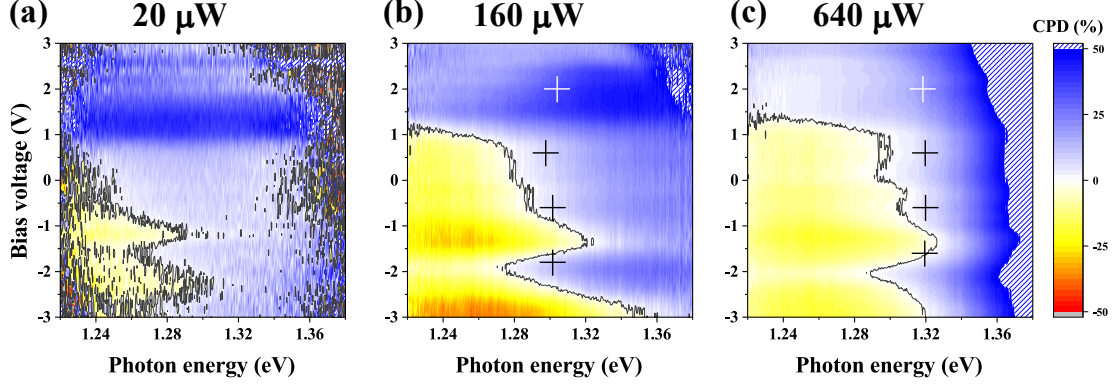


Figure 4.11: Contour plots of CPD values with  $d_B = 10$  nm as a function of excitation power: (a) 20  $\mu\text{W}$ , (b) 160  $\mu\text{W}$ , and (c) 640  $\mu\text{W}$ , respectively. White and black crosses in (b) and (c) indicate the PL intensity peak position of the oscillation behavior, as shown in Fig. 4.10 (b) and (c), respectively.

In the spin injection process into QDs, the majority spin states of electrons at the GSs can be easily filled because of those limited densities; therefore, the further injection can be blocked by the Pauli exclusion principle. In contrast, minority spins can be continuously injected and reduce the spin polarization at the GSs, particularly at high excitation powers. The bias region showing negative CPDs (anti-parallel spin to the initial spin direction) becomes broader at high powers, as shown in Fig. 4.11 (b) and (c), than that at the lowest power, as shown in Fig. 4.11 (a). The negative CPD value indicates the maximum of  $-40\%$  at 160  $\mu\text{W}$ , as shown in Fig. 4.11 (b). As pointed out earlier in Fig. 4.9 (b), the negative CPD values weakened around the biases indicate stronger PL intensities, which were and are depicted by cross marks in Fig. 4.11 (b) and (c) and is also discussed later.

The most important finding of this study is the existence of specific biases showing high positive CPD values sufficiently identifiable from the background positive CPDs; thus, the existence of bias conditions enabling highly efficient spin injection, as shown in Fig. 4.9 (a)–(c) and Fig. 4.11 (a)–(c). To verify this enhanced spin-injection chan-

nel, coupled electron wavefunctions spreading over this QD–QW tunneling structures were calculated [116]. The calculation model was created based on our structural observations using a cross-sectional TEM and scanning AFM [110, 136]. The In concentration distribution inside the QD was also taken into account [137]. I found the existence of strong coupling of the electron wavefunction between ESs of the QW and QD across the tunneling barrier at a bias voltage of +1.2 V, typically as shown in Fig. 4.12 (a). This strong coupling originates from a resonant state between the 2D-QW and 0D-QD via a 2D wetting layer (WL), as shown in Fig. 4.12 (b); the WL has the same dimensionality as the QW and can enhance the penetration of 2D-QW wave function, as well as the close distance to the QD. Owing to the existence of the WL in self-assembled QDs, the deep penetration of the electron wave function into QD ESs can open an efficient spin injection path, because of the faster injection than spin relaxation inside the 2D-QW.

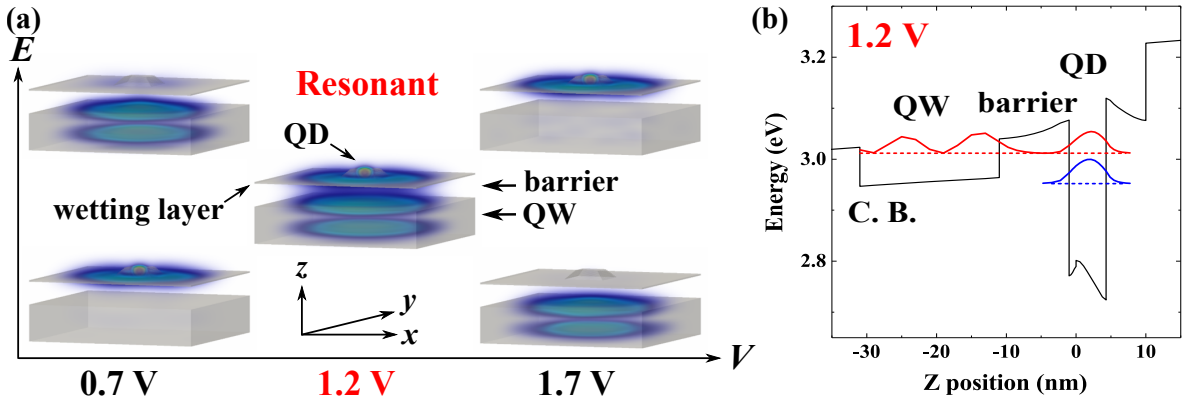


Figure 4.12: (a) 3D-calculation result of the electron wavefunction of the coupled nanostructure with  $d_B = 10$  nm as a function of bias voltage around +1.2 V (resonant condition). Energy relations (vertical axis) among each wavefunction are schematically expressed, where the off-resonant states at 0.7 and 1.7 V show anti-bonding. (b) Electron-wavefunction calculation along the growth direction of the coupled nanostructure with a bias voltage of +1.20 V. A red solid line indicates the strongly coupled state, blue solid lines show the GS of QD, respectively. Broken lines show the corresponding eigenvalues.

After tunneling, the spin-polarized electron can immediately relax to the lower energy states in the QDs, such as the GS and several ESs just above the GS, depending

on the degree of the state filling. Recently, a clear effect of the phonon bottleneck has been reported in a similar coupled InGaAs QD-QW nanosystem [138]. Energy relaxation involving longitudinal optical (LO)-phonon scattering of a zone holding mode as well as a  $\Gamma$ -point mode was observed to enhance the PL intensity from emissive states transitioned by energy relaxation [139–142].

From the above consideration taking resonant tunneling into account, I discuss characteristic oscillation behaviors of the PL intensity as a function of bias, as shown in Fig. 4.8 (b) and 4.10 (b)–(c). The bias dependence of the CPD as indicated by cross symbols in Fig. 4.9 (b) and 4.11 (a)–(c) is also discussed.

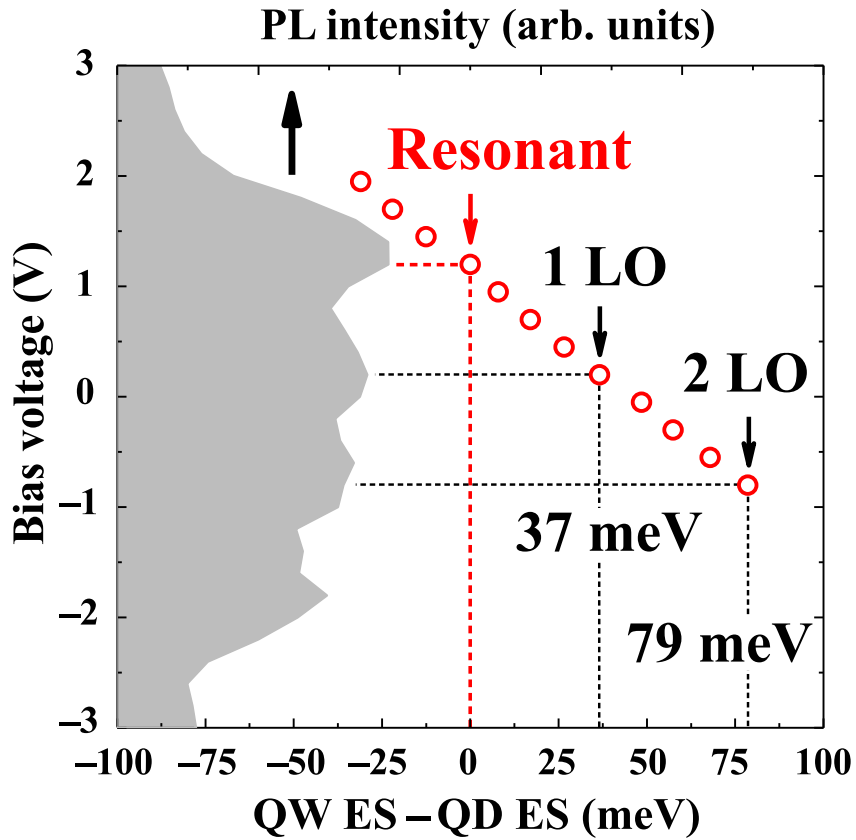


Figure 4.13: Energy difference between the coupled ES in the QW and that in the QD side (red open circles), and the PL intensity (a grey region), as a function of bias with  $P_{exc} = 40 \mu\text{W}$ , where 1 or 2 LO-phonon energy difference from the resonant coupling energy at the 1.2 V is expressed by a narrow black arrow.

As noted above, around the bias voltage of +1.2 V, the efficient tunneling paths open, and spin-polarized electrons can be efficiently injected. One can consider LO-phonon mediated resonant tunneling when a more negative voltage is applied. The coupled excited states of the QD involving the WL shifts toward the lower energy side compared to the coupled ES energy in the QW side under the application of more negative bias. This energy difference was also calculated as a function of bias, as shown in Fig. 4.13. I find that the PL-intensity oscillation peak agrees well with the situation at which the bias application makes the energy difference between the above QW and QD coupled ESs just 1 or 2 LO-phonon energy (Fig. 4.13). This means that an efficient quasi-resonant tunneling path involving LO-phonon scattering can be formed, when the energy difference between the coupled states of the QD-WL, and QW becomes 1 or 2 LO-phonon energy [138]. Therefore, I conclude that parallel spins can be efficiently injected at those biases, which significantly enhance the positive CPD values and also weaken the negative CPD values indicated by the cross symbols in Fig. 4.8 (b) and 4.10 (b)-(c).

## 4.4 Summary

In summary of this chapter, electric-field effects on the QD-PL intensity and CPD after spin injection from the QW have been observed using high-density un-doped InGaAs QDs tunnel-coupled with a 2D QW. The electric field is applied along the QD-QW growth direction in combination with varying the tunneling barrier thickness. Characteristic resonant coupling between the 2D-QW and 0D-QD ESs can be formed through a 2D WL at a specific bias condition, resulting in efficient parallel spin injection without a significant loss of the spin polarization. Effects of LO-phonon scattering during the spin injection process into the QDs are newly observed. The PL-intensity oscillation [Fig. 4.14 (a)] can be explained taking LO-phonon emissions

into account. As a result, highly efficient spin injection with the degree of circular polarization (photon spin) higher than 36% is achieved, even at GSs of the QD ensemble after the injection [below Fig. 4.14 (b)]. This condition is sensitive to both the electric field strength and the tunneling barrier thickness, as well as the excitation spin density. These experimental findings realizing such a highly efficient optical spin injection into QDs will motivate to design coupled quantum structures suitable for optical devices and photo-electric information processing based on the spin polarization.

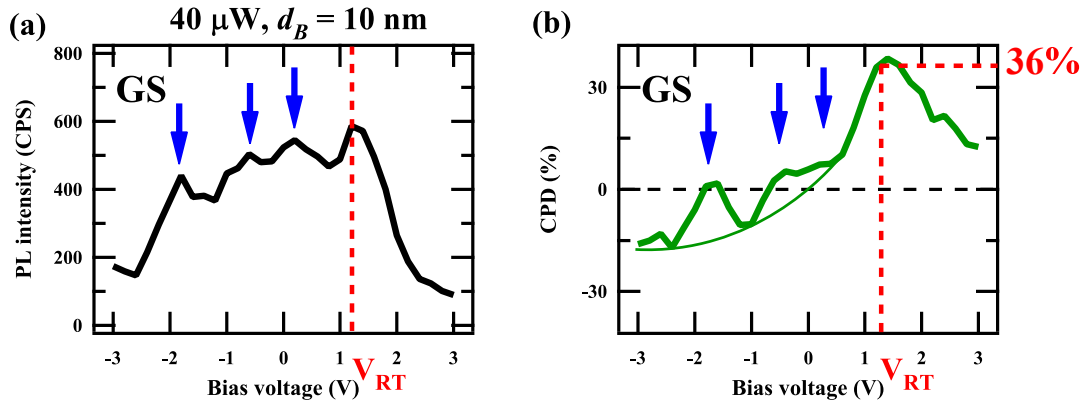


Figure 4.14: (a) QD-PL intensity and (b) the corresponding CPD values at the photon energy of 1.28 eV as a function of bias for the sample with  $d_B = 10$  nm under an excitation power of  $40 \mu\text{W}$ .  $V_{RT}$  indicates a bias voltage to realize a resonant tunneling phenomenon between the 2D-QW and 0D-QD ESs via a 2D-WL. A narrow green line is guide for the eyes.

# Chapter 5

## Electric-field effects on spin-injection polarity and the spin-polarization degree in QD

### 5.1 Electric-field effects on electron-spin polarity during spin injection

Figures 5.1(a, b) show contour plots of the QD-PL intensity and the corresponding CPD values as functions of photon energy and bias voltage under  $\sigma^-$  excitation.

Figure 5.1 (c, d) shows circularly polarized PL spectra for the un-doped QD sample with an excitation power of  $320 \mu\text{W}$  under bias voltages of 0 (c) and 1.0 V (d). The ground states (GSs) of this high-density QD ensemble can be identified from a sufficiently lower excitation power of  $10 \mu\text{W}$ . Significant negative CPD (cross-circular, anti-parallel spin to the initial QW spin) values down to  $-29\%$  are observed only at the GSs with 0 V, as shown in Fig. 5.1 (c), while excited states (ESs) above 1.33 eV show positive CPDs (co-circular, parallel spin resulting from efficient spin injection).

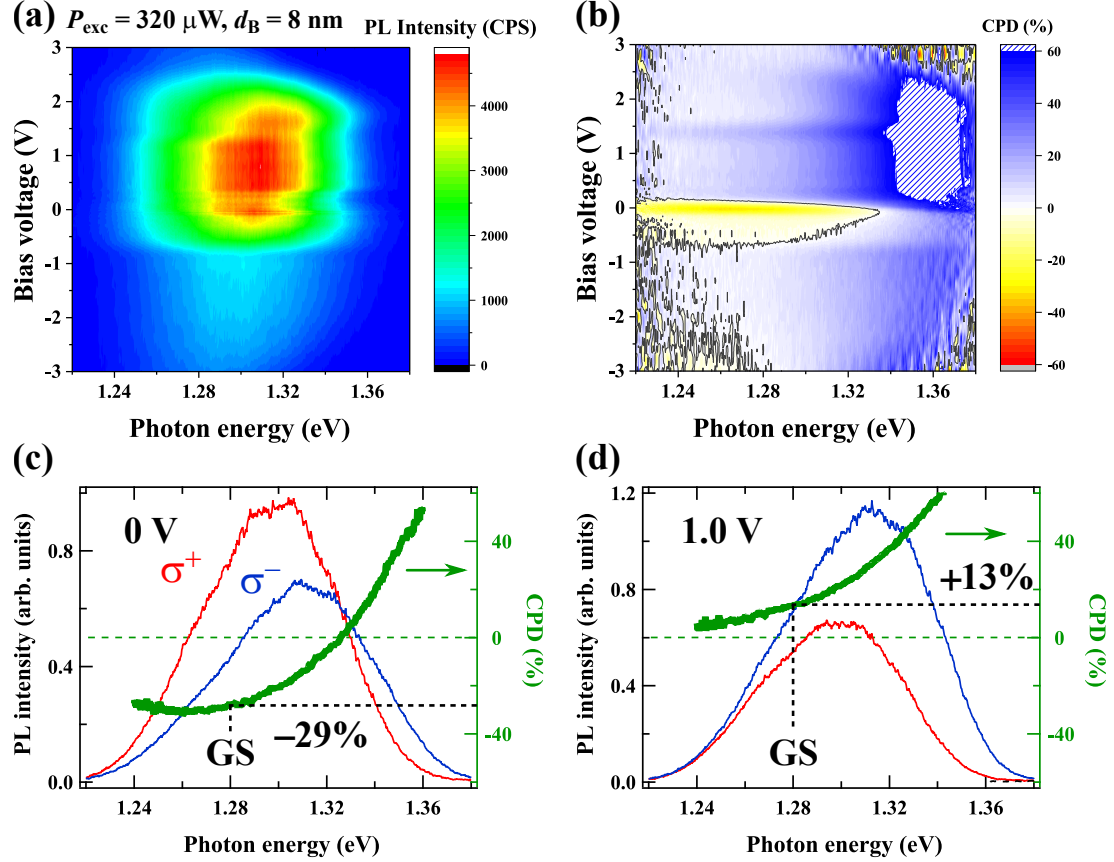


Figure 5.1: Contour plots of the QD-PL intensity (a) and the corresponding CPD values (b) as functions of photon energy and bias voltage under  $\sigma^-$  excitation in the un-doped QD sample with  $d_B = 8$  nm. Circularly polarized PL spectra (co-circular  $\sigma^-$ : a blue line, cross-circular  $\sigma^+$ : a red line, and the corresponding CPD value: a green line) at 4 K under  $\sigma^-$  excitation for the QW with 0 V (c) and 1.0 V (d).

In contrast, a positive CPD property (co-circular, parallel spin) is dominant even at the GS with 1.0 V, as shown in Fig. 5.1 (d).

A clear bias region from  $-0.7$  to  $0.1$  V exhibiting negative CPD values can be observed, which was mentioned in the previous chapter. This indicates an anti-parallel spin state in the QDs against for the initial QW-spin direction. These negative CPDs disappear at the higher energy side corresponding to the ESs.

Circularly polarized transient PL and the corresponding CPD from the QD-GS are shown with a bias voltage of 0 V [Fig. 5.2 (a)] and 1.0 V [Fig. 5.2 (b)]. A drastic change in the time-dependent CPD property is observed at this bias condition, where

significant negative CPD values gradually develop from almost 0 at the beginning to  $-40\%$  after 2.0 ns. In contrast, marked initial positive polarizations up to 30% appear at 1.0 V and then decrease steeply within 0.2 ns.

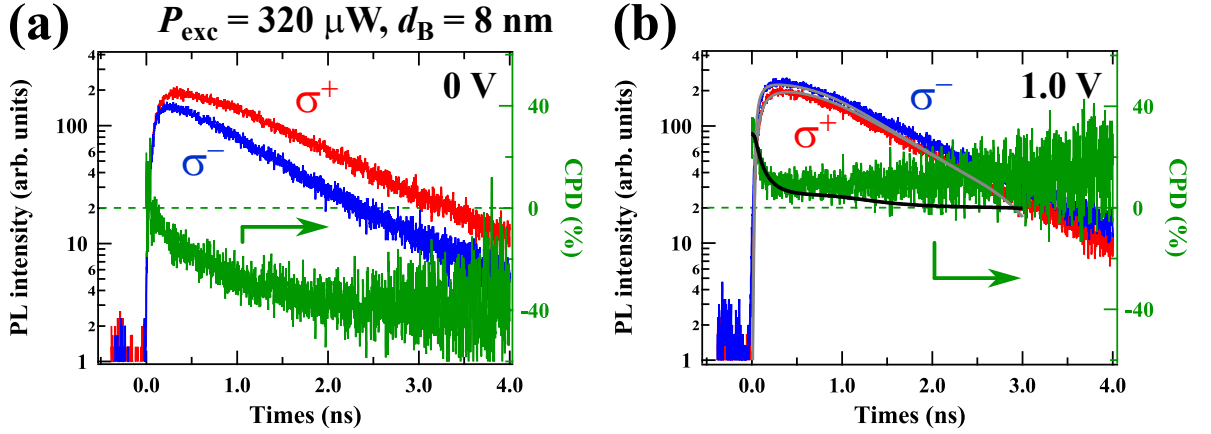


Figure 5.2: Circularly polarized time-resolved PL responses at the GS (1.28 eV) in the un-doped QD sample, at 4 K with 0 V (a) and 1.0 V (b) under the QW- $\sigma^-$  excitation of  $320 \mu\text{W}$ .

Negative CPD (cross-circular polarization) properties were previously observed by formation of negatively charged excitons (trions) with excess electrons in QDs [115, 130–133, 135, 143], while positively charged trions with excess holes can show co-circular polarization. Several mechanisms based on the negative trion formation have been proposed to explain the negative PL polarization. A spin flip-flop transition via electron-hole scattering at ESs in QDs was discussed [131]. The relatively slow development of the negative CPD as shown in Fig. 5.2 was also observed in the negative trion formation phenomenon [131, 135]. An effect of dark exciton accumulation was also observed [132]. Spin-polarized light excitation in a QW produced a mixture of bright and dark excitons depending on the degree of hole-spin relaxation. Negative trions were able to be formed in QD-like wider QW parts with lower energies and residual electrons by capturing the dark excitons. Effects of excitation power density and  $p$ -doping were studied, where higher excitation powers enhanced a negative CPD

value and that enhancement correlated with increasing emission intensity from the ESs [133,135].

The observation of the negative CPD (cross-circular polarization) values in the present QW/QD nanostructure can be discussed based on the trion formation in QDs [115]. Puttison et al. have reported positive trion ( $X^+$ ) and negative trion ( $X^-$ ) formations with co- and cross-circular polarizations of QD-PL emissions.

They showed a fitting model assuming overlapped  $X^+$  and  $X^-$  PL emission bands for the QD-PL spectra of the QD ensemble [115]. Two PL emission bands originating from the trion formation with a similar spectral lineshape were assumed. The experimental results of QD-PL can be understood by a sum of these two PL bands with splitting energy of 9 meV.

The electric field effect on the reversal of spin polarity in our spin-injection process can be interpreted based on the above trion formation. Electrons and holes can be smoothly injected from the QW into the QDs around 1 V, which is indicated by the bright PL as shown in Fig. 5.1 (a). However, around 0 V, the calculated valence band potentials of the QW, as well as a barrier between the QW and QD, prevent the smooth injection of hole. The holes are likely to localize in the QW region opposite from the QD side. On the other hand, electrons localize in the QW close to the QD side and then can efficiently tunnel to the QDs. Besides, the electron has a lower effective mass than that of the hole. As a result, negative trions can be formed in the QDs. Therefore, the spin polarity of electrons injected from the QW can be switched by application of external electric fields. The abovementioned negative trion formation through the electric field can be controlled by potential modifications between these characteristic 2D QW and 0D QD.

This trion picture and the resultant spin polarity in the spin injection process from the QW to QDs are supported by the  $p$ -doping effect. The  $p$ -doping effect will be discussed later.

Here, I briefly explain how the negative PL-CPD arises in our QW/QD samples, depending on the electric field [131, 144].

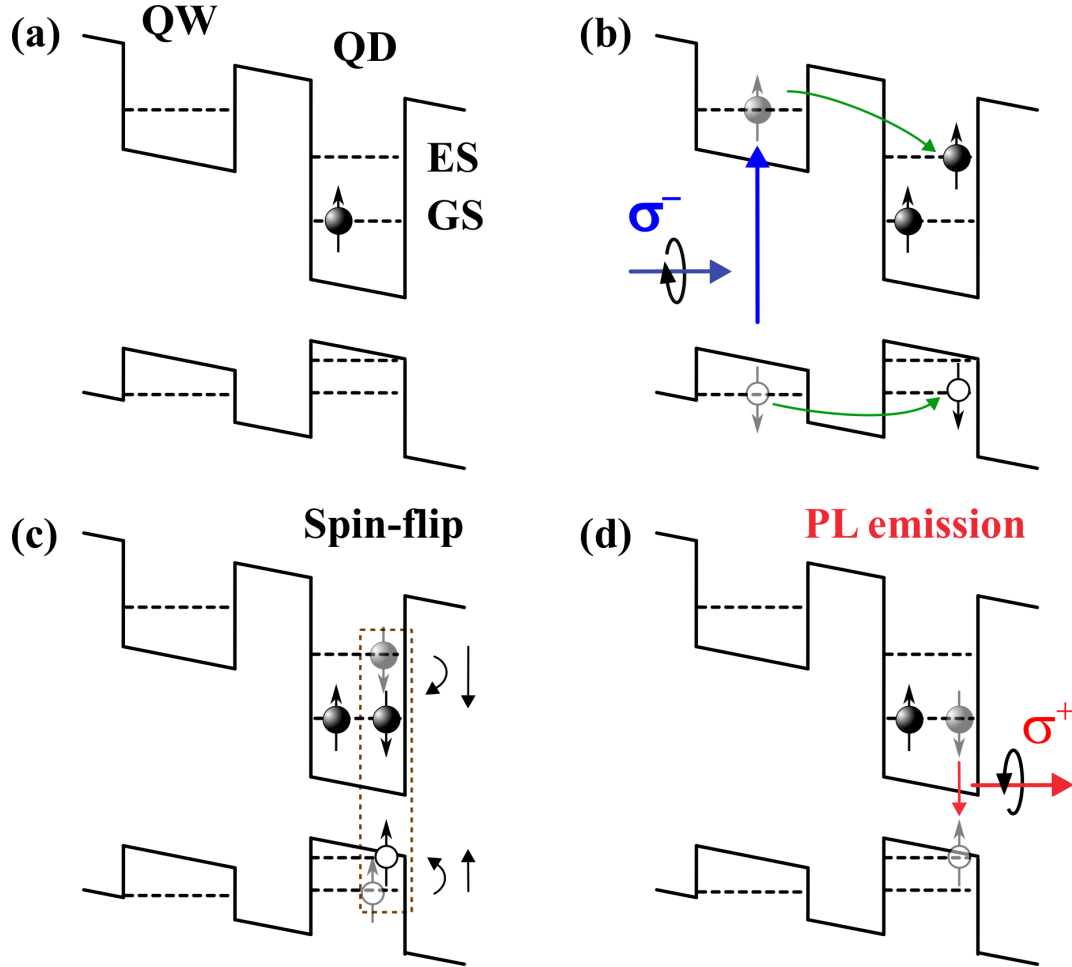


Figure 5.3: A schematic drawing of the spin-flip process to explain the circularly polarized PL with negative CPDs, observed in the present QW/QDs coupled nanostructure.

For simplicity, I assume that one QD is occupied by one spin-polarized residual electron at the GS. An electron-hole pair in the QW can then be transferred into the QD-ES after the QW excitation via tunneling. The subsequent relaxation to the GS inside the QD can be blocked by the residual electron due to Pauli blocking if this residual electron has a parallel-spin orientation to the latter injected electron. Therefore, the electron-hole pair occupies the ES and the electron spin in this ES induces a simultaneous spin-flip transition [131]. After this spin-flip transition, the

anti-parallel electron spin for the first residual electron can relax to the GS. The electron-hole pair at the GS can recombine and the cross-circular polarization PL ( $\sigma^+$ ) emitted. As a result, the CPD with negative CPD (anti-parallel spin for the initial one in the QW) appears.

### 5.1.1 Excitation-power dependence of CPD property

Figure 5.4 shows an averaged CPD value in the un-doped GS-PL as a function of excitation light power ( $P_{exc}$ ).

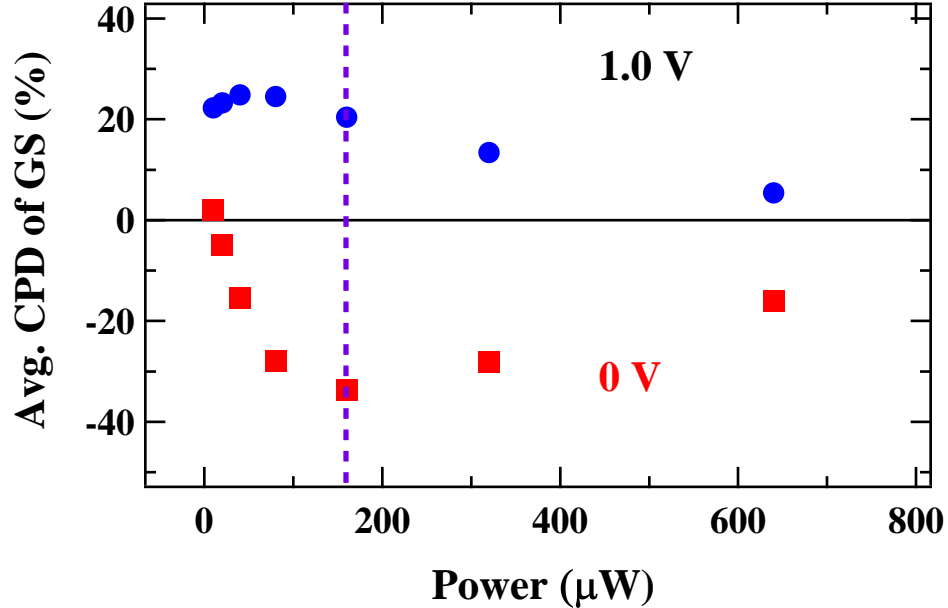


Figure 5.4: Averaged CPD value in the QD-GSs (1.27–1.29 eV) as a function of excitation light power under  $\sigma^-$  excitation at 4 K with bias voltages of 0 V (a red closed square) and 1.0 V (a blue closed circle).

At 1.0 V, high values of positive CPD are observed in a low  $P_{exc}$  region less than 160  $\mu\text{W}$  and then gradually decrease toward to 0 with increasing  $P_{exc}$ . In contrast, a negative CPD significantly develops at 0 V with increasing  $P_{exc}$  in this low  $P_{exc}$  region, reaching the minimum at  $P_{exc} = 160 \mu\text{W}$ . Beyond 160  $\mu\text{W}$ , the CPD tends to gradually approach 0 with increasing  $P_{exc}$ . The former  $P_{exc}$  dependence of the positive CPD at 1.0 V can be well explained by a state filling effect at the discrete density

of the spin-split states in the QD. Spin-polarized electrons can be injected from the QW into the QDs and show co-circular polarization for the initial spin state in the QW under relatively low excitation-power conditions. By increasing the number of excitation spins, the majority (co-circular) spin states in the QD ensemble are fully occupied and further spin injection ceases due to Pauli spin blocking [89, 90]. However, the minority spins can be continuously injected causing the spin polarization in the QD ensemble to decrease by increasing the number of excitation spins [87, 88]. On the other hand, scattering at ESs causes the abovementioned electron-spin flip, thus explaining the excitation-power dependence of the positive CPD at 1.0 V. According to this spin-flip scenario, the initial development of the negative CPD with increasing  $P_{exc}$  at 0 V can be reasonably explained by increasing the residual electron occupation at GSs in the QD ensemble. Further suppression of this negative CPD as  $P_{exc}$  increases beyond 160  $\mu\text{W}$  can also be understood by multiple electron-spin scattering among several ESs in the QDs. This may induce complicated scattering and thus randomizes the total spin polarization through the multiple spin-flip processes. The previous dark exciton model indicated a monotonic increase only in the negative CPD with increasing excitation power, and further electron doping reduced the negative CPD [132]. We have observed the existence of optimum excitation power for achieving the maximum value of negative CPD, as shown in Fig. 5.4. The degree of spin polarization for both spin polarities depending on the bias is maximized by the existence of this optimized excitation-spin density at 160  $\mu\text{W}$ . Therefore, spin switching efficiency can be optimized by the combination of excitation-spin density and external bias application. Time-resolved PL in the QDs indicates that the CPD decay time of ESs becomes faster at 0 V [Fig. 5.5 (b)], at which negative CPD at the GS [Fig. 5.5 (a)] is markedly observed. On the other hand, the CPD decay is slower in ESs at 1 V [Fig. 5.5 (c)], at which bias the positive CPD is observed at the GS. Spin scattering accompanying spin flip can enhance the spin relaxation rate at the

ESs when excess electrons exist at ESs, while the PL decay times are identical. This acceleration of spin relaxation at the ESs under 0 V suggests an important role of QD excited spin states for this reversal of spin polarity at the GS, after spin injection from the QW.

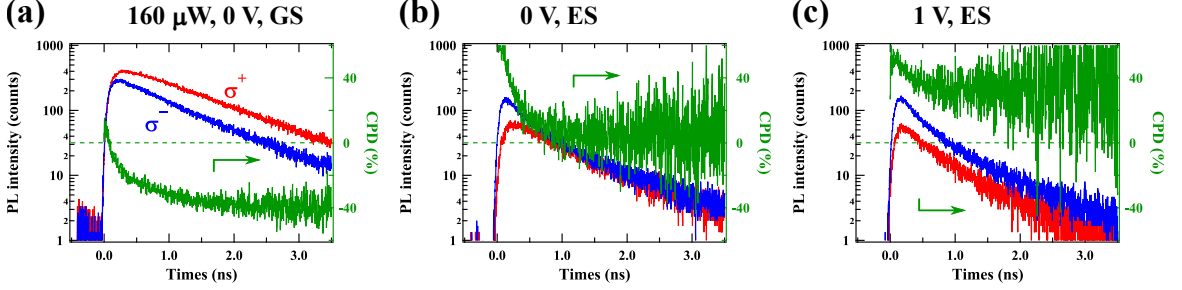


Figure 5.5: Circularly polarized time-resolved PL responses at 4 K in the un-doped QD sample, at the GS (1.28 eV) with 0 V (a), at the ES (1.34 eV) with 0 V (b), and the ES with 1 V (c), under the QW- $\sigma^-$  excitation of 160  $\mu\text{W}$ .

## 5.2 Effects of $p$ -doping in QDs

### 5.2.1 Effects of $p$ -doping on QD-PL intensity

$P$ -doped QD samples were prepared with Be concentrations of  $1 \times 10^{17} \text{ cm}^{-3}$  and  $3 \times 10^{17} \text{ cm}^{-3}$  in the GaAs capping layer, respectively.

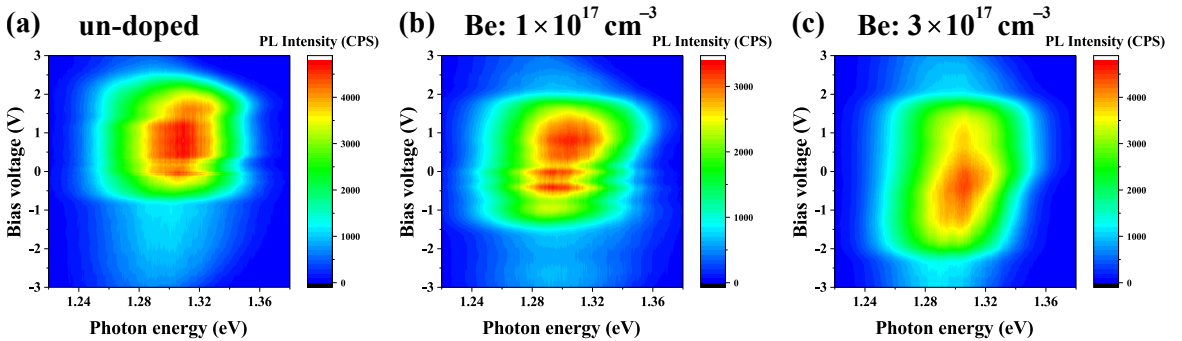


Figure 5.6: Contour plots of PL intensity at 4 K as functions of photon energy and bias voltage with the QW excitation power of 320  $\mu\text{W}$ , in (a) un-doped QDs,  $p$ -doped QD samples with a lower (b) and higher (c) doping concentrations, respectively. The barrier thickness is 8 nm.

Figures 5.6 (a)-(c) show contour plots of QD-PL intensity as functions of photon energy and bias voltage in (a) un-doped QDs, low  $p$ -doped, and high  $p$ -doped QD samples. High PL intensities are observed ranging from +2.0 V to  $-0.5$  V for the un-doped sample. This bias region gives a nearly flat-band potential condition based on potential calculations. This strong PL intensity region is extended ranging from +2.0 to  $-1.5$  V and +2.0 to  $-2.5$  V for the lower and higher  $p$ -doping conditions, respectively. This extended bias region toward the negative bias direction can be explained by compensation for the absence of hole injection with biases less than  $-1.0$  V. The Be doping can produce the desired number of residual hole into the QDs [Fig. 5.7 (a)]. However, the QD-PL decreases with further increasing of negative bias from  $-2.5$  V, due to the hole escape from the QDs to the QW [Fig. 5.7 (b)].

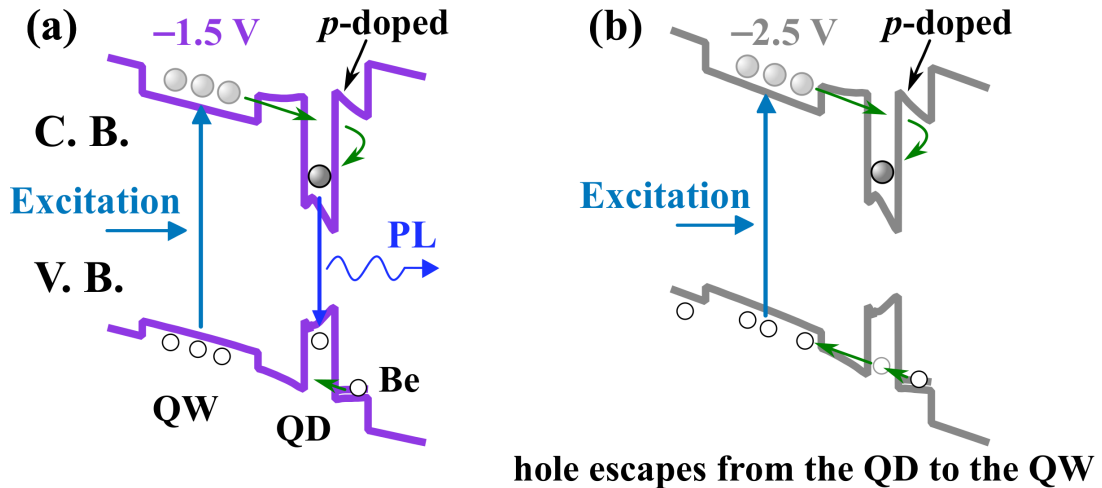


Figure 5.7: 3D-calculated energy-band structures and the schematic drawing of hole dynamics at (a)  $-1.5$  V and (b)  $-2.5$  V.

## 5.2.2 Effect of $p$ -doping on circular polarization property of PL

Figures 5.8 (a)-(c) show effects of the  $p$ -doping on contour plots of the corresponding CPD value of the QD-PL. Positive CPD values ranging from 20% to 30% were

observed with positive bias application for all samples, indicating a parallel spin injection from the QW.

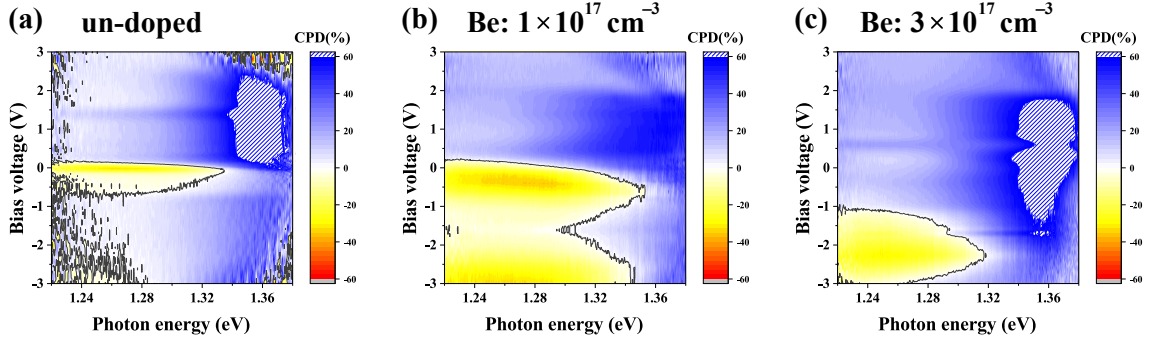


Figure 5.8: Contour plots of a CPD value of the QD-PL at 4 K as functions of photon energy and bias voltage in (a) the un-doped QD, (b) low  $p$ -doped QD, and (c) high  $p$ -doped samples. A black narrow solid line expresses CPD = 0%. A red hatched area corresponds to the region with positive CPD  $\geq 60\%$ .

The strong negative CPD region around 0 V is observed in the un-doped and  $p$ -doped sample with a lower Be concentration as shown in Fig. 5.8 (a) and (b). This bias region with negative CPDs is largely affected by heavy  $p$ -doping in QDs, as shown in Fig. 5.8 (c). The biases exhibiting the negative CPD properties shift to the more negative bias side and this bias region becomes significantly broader. Excess holes provided by  $p$ -doping can prevent to form negative trions. Therefore, stronger negative bias application is necessary to induce the negative trion formation with the negative CPD. This condition can be accomplished through the higher tunneling probabilities of an electron resulting from the potential modifications. The broad bias region indicating this negative CPD can be explained by inhomogeneous distribution of the number of doped hole in the QD ensemble.

### 5.3 Summary

In summary of this chapter, electric-field effects of optical spin injection into un-doped and  $p$ -doped InGaAs QDs in tunnel-coupled InGaAs QW/QDs nanosystems

have been studied by modifying the tunnel-coupled potential, as shown in Fig. 5.9. The spin polarity can be switched between parallel and anti-parallel to the initial spin direction in the QW by simply applying an external bias, as shown in Fig. 5.9 (b). The switching bias for the spin polarity shifts to a more negative bias side and the bias region becomes broader by higher concentration  $p$ -doping in QDs, as shown in Fig. 5.9 (d). The bias dependence of the spin polarity can be explained in terms of bias induced selective formation of negatively or positively charged trions during the spin-injection process from the QW into the QDs in these QW/QDs coupled nanostructures. I show that the efficiency of this spin switching can be maximized and thus optimized by the excitation-spin density. Electric-field control of the spin injection dynamics and the resultant spin states in high-density QDs will contribute to semiconductor spintronics such as an optical device and photoelectric information processing based on the spin polarization.

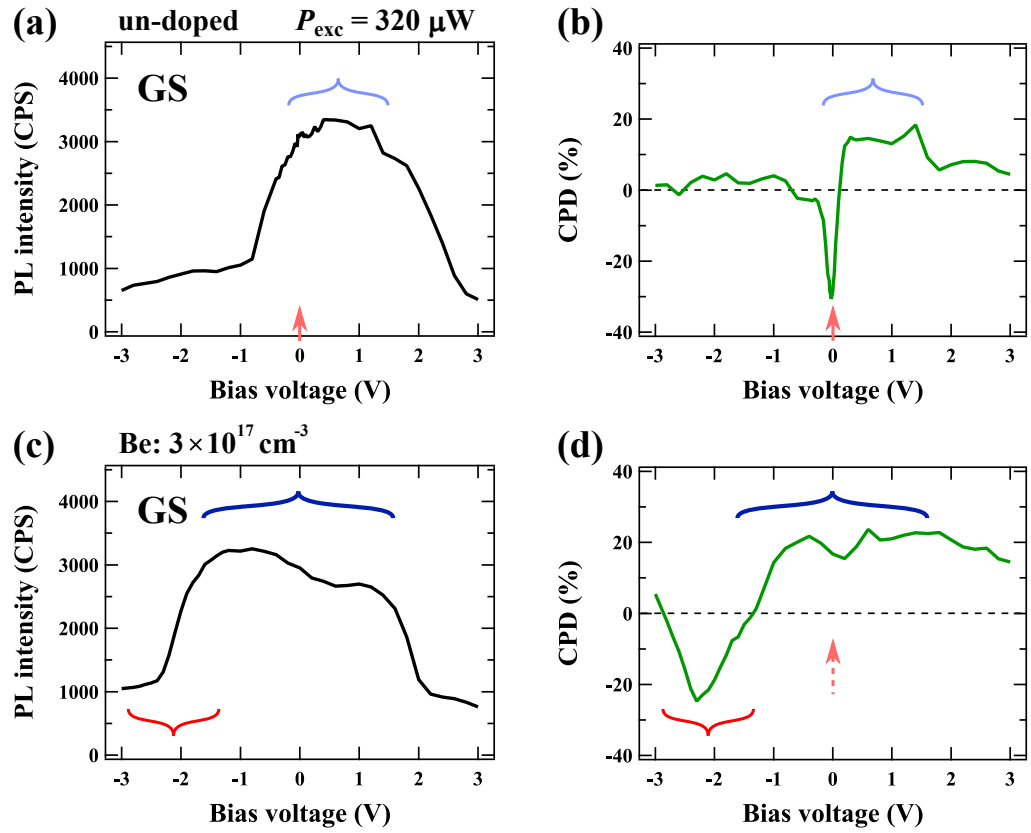


Figure 5.9: QD-PL intensity at the photon energy of 1.28 eV as a function of bias under an excitation power of  $320 \mu\text{W}$  in un-doped (a) and high  $p$ -doped QD samples (c) with  $d_B = 10 \text{ nm}$ . The corresponding CPD values in the un-doped sample (b) and high  $p$ -doped QD samples (d).

# Chapter 6

## Conclusion

Based on my research work, electric-field effects on optical electron-spin injection in quantum well (QW)/quantum dots (QDs)-coupled nanostructures have been elucidated as follows:

1: Efficient electron-spin injection from the QW to the ground state (GS) of the QD was found by changing the electric field strength, which can be sustained by resonant tunneling via a wetting layer and LO-phonon scattering.

After the spin injection, parallel spin states to the initial spin direction in the QW were observed in QDs with wide bias range as a result of the efficient spin injection. The most important finding is the existence of specific bias (+1.2 V) showing the highest positive CPD values (>39%) sufficiently identifiable from the background positive CPDs (~20%) corresponding to normal spin injection. The existence of this bias condition enabling highly efficient spin injection can be interpreted by characteristic resonant tunneling between the 2D QW and 0D QDs via a 2D wetting layer. Moreover, the QD-PL intensity and the corresponding positive CPD values are markedly enhanced, when the bias application made an energy difference between the coupled ES in the QW and that in the QD just 1 to 3 LO-phonon energy.

2: The spin-injection polarity can be controlled by applying an external bias.

Significant electric-field effects on the reversal of spin polarity were observed at the QD-GS (CPD  $\sim -40\%$ ) in the spin-injection process from the QW. The tunneling rate of an electron is different from that of a hole and largely depends on the electric field strength, owing to electric-field induced modifications of the coupled QD-QW potential. This results in negative trions in the QDs with anti-parallel electron spins to the initial electrons in the QW, which is supported by a significant effect of  $p$ -doping into the QDs. The CPD of both spin polarities can be optimized by excitation-spin density, in addition to the electric field strength.

# Bibliography

- [1] C. Kittel, P. McEuen, and P. McEuen. *Introduction to solid state physics*. Wiley New York, (1976).
- [2] J. H. Davies. *The physics of low-dimensional semiconductors: An introduction*. Cambridge university press, (1998).
- [3] D. D. Awschalom, D. Loss, and N. Samarth. *Semiconductor spintronics and quantum computation*. Springer Science & Business Media, (2013).
- [4] M. I. Dyakonov. *Spin physics in semiconductors*. Springer, (2008).
- [5] Y. Ohno, D. K. Young, B. Beschoten, F. Matsukura, H. Ohno, and D. D. Awschalom. Electrical spin injection in a ferromagnetic semiconductor heterostructure. *Nature*, **402**(6763):790, (1999).
- [6] G. Schmidt, D. Ferrand, L. W. Molenkamp, A. T. Filip, and B. J. van Wees. Fundamental obstacle for electrical spin injection from a ferromagnetic metal into a diffusive semiconductor. *Physical Review B*, **62**(8):R4790, (2000).
- [7] J. R. Petta, A. C. Johnson, J. M. Taylor, E. A. Laird, A. Yacoby, M. D. Lukin, C. M. Marcus, M. P. Hanson, and A. C. Gossard. Coherent manipulation of coupled electron spins in semiconductor quantum dots. *Science*, **309**(5744):2180, (2005).
- [8] X. H. Lou, C. Adelmann, S. A. Crooker, E. S. Garlid, J. J. Zhang, S. M. Reddy, S. D. Flexner, C. J. Palmstrøm, and P. A. Crowell. Electrical detection of spin transport in lateral ferromagnet–semiconductor devices. *Nature Physics*, **3**(3):197, (2007).
- [9] S. Datta and B. Das. Electronic analog of the electro-optic modulator. *Applied Physics Letters*, **56**(7):665, (1990).
- [10] J. Nitta, T. Akazaki, H. Takayanagi, and T. Enoki. Gate control of spin-orbit interaction in an inverted  $\text{In}_{0.53}\text{Ga}_{0.47}\text{As}/\text{In}_{0.52}\text{Al}_{0.48}\text{As}$  heterostructure. *Physical Review Letters*, **78**(7):1335, (1997).
- [11] P. Recher, E. V. Sukhorukov, and D. Loss. Quantum dot as spin filter and spin memory. *Physical Review Letters*, **85**(9):1962, (2000).

- [12] C. Reig, S. Cardoso, and S. C. Mukhopadhyay. *Giant magnetoresistance (GMR) sensors*. Springer, (2013).
- [13] Y. Ando. Spintronics technology and device development. *Japanese Journal of Applied Physics*, **54**(7):070101, (2015).
- [14] A. Hirohata and K. Takanashi. Future perspectives for spintronic devices. *Journal of Physics D: Applied Physics*, **47**(19):193001, (2014).
- [15] M. N. Baibich, J. M. Broto, A. Fert, F. N. Van Dau, F. Petroff, P. Etienne, G. Creuzet, A. Friederich, and J. Chazelas. Giant magnetoresistance of (001)Fe/(001)Cr magnetic superlattices. *Physical Review Letters*, **61**(21):2472, (1988).
- [16] G. Binasch, P. Grünberg, F. Saurenbach, and W. Zinn. Enhanced magnetoresistance in layered magnetic structures with antiferromagnetic interlayer exchange. *Physical Review B*, **39**(7):4828, (1989).
- [17] T. Miyazaki and N. Tezuka. Giant magnetic tunneling effect in Fe/Al<sub>2</sub>O<sub>3</sub>/Fe junction. *Journal of Magnetism and Magnetic Materials*, **139**(3):L231, (1995).
- [18] S. A. Wolf, D. D. Awschalom, R. A. Buhrman, J. M. Daughton, S. Von Molnar, M. L. Roukes, A. Y. Chtchelkanova, and D. M. Treger. Spintronics: a spin-based electronics vision for the future. *Science*, **294**(5546):1488, (2001).
- [19] I. Žutić, J. Fabian, and S. D. Sarma. Spintronics: Fundamentals and applications. *Reviews of Modern Physics*, **76**(2):323, (2004).
- [20] D. D. Awschalom, D. Loss, and M. Samarth. *Spintronics Semiconductor and Computation Quantum*. Springer, Berlin, 2002.
- [21] R. von Helmolt, J. Wecker, B. Holzapfel, L. Schultz, and K. Samwer. Giant negative magnetoresistance in perovskitelike La<sub>2/3</sub>Ba<sub>1/3</sub>MnO<sub>x</sub> ferromagnetic films. *Physical Review Letters*, **71**(14):2331, (1993).
- [22] J. S. Moodera, L. R. Kinder, T. M. Wong, and R. Meservey. Large magnetoresistance at room temperature in ferromagnetic thin film tunnel junctions. *Physical Review Letters*, **74**(16):3273, (1995).
- [23] S. Ikeda, J. Hayakawa, Y. Ashizawa, Y. M. Lee, K. Miura, H. Hasegawa, M. Tsunoda, F. Matsukura, and H. Ohno. Tunnel magnetoresistance of 604% at 300 K by suppression of Ta diffusion in CoFeB/MgO/CoFeB pseudo-spin-valves annealed at high temperature. *Applied Physics Letters*, **93**(8):082508, (2008).
- [24] B. Dieny, V. S. Speriosu, S. S. P. Parkin, B. A. Gurney, D. R. Wilhoit, and D. Mauri. Giant magnetoresistive in soft ferromagnetic multilayers. *Physical Review B*, **43**(1):1297, (1991).

- [25] N. F. Mott. The electrical conductivity of transition metals. *Proceedings of the Royal Society of London. Series A-Mathematical and Physical Sciences*, **153**(880):699, (1936).
- [26] S. M. Thompson. The discovery, development and future of GMR: The Nobel Prize 2007. *Journal of Physics D: Applied Physics*, **41**(9):093001, (2008).
- [27] P. Chen, J. Moser, P. Kotissek, J. Sadowski, M. Zenger, D. Weiss, and W. Wegscheider. All electrical measurement of spin injection in a magnetic  $p-n$  junction diode. *Physical Review B*, **74**(24):241302, (2006).
- [28] M. E. Flatte and G. Vignale. Unipolar spin diodes and transistors. *Applied Physics Letters*, **78**(9):1273, (2001).
- [29] M. E. Flatté, Z. G. Yu, E. Johnston-Halperin, and D. D. Awschalom. Theory of semiconductor magnetic bipolar transistors. *Applied Physics Letters*, **82**(26):4740, (2003).
- [30] E. I. Rashba. Properties of semiconductors with an extremum loop. I. Cyclotron and combinational resonance in a magnetic field perpendicular to the plane of the loop. *Soviet Physics, Solid State*, **2**:1109, (1960).
- [31] E. I. Rashba and I. I. Boiko. Properties of semiconductors with an extremum loop. II. Magnetic susceptibility in a field perpendicular to the plane of the loop. *Soviet Physics, Solid State*, **2**:1692, (1960).
- [32] E. I. Rashba and I. I. Boiko. The properties of semiconductors with extremum loops. III. Behavior in magnetic field parallel to the plane of the loop. *Soviet Physics, Solid State*, **3**:927, (1960).
- [33] Y. A. Bychkov and E. I. Rashba. Oscillatory effects and the magnetic susceptibility of carriers in inversion layers. *Journal of Physics C: Solid State Physics*, **17**(33):6039, (1984).
- [34] J. Luo, H. Munekata, F. F. Fang, and P. J. Stiles. Effects of inversion asymmetry on electron energy band structures in GaSb/InAs/GaSb quantum wells. *Physical Review B*, **41**(11):7685, (1990).
- [35] T. Koga, J. Nitta, T. Akazaki, and H. Takayanagi. Rashba spin-orbit coupling probed by the weak antilocalization analysis in InAlAs/InGaAs/InAlAs quantum wells as a function of quantum well asymmetry. *Physical Review Letters*, **89**(4):046801, (2002).
- [36] T. Koga, J. Nitta, H. Takayanagi, and S. Datta. Spin-filter device based on the Rashba effect using a nonmagnetic resonant tunneling diode. *Physical Review Letters*, **88**(12):126601, (2002).

- [37] S. Souma, A. Sawada, H. Chen, Y. Sekine, M. Eto, and T. Koga. Spin blocker using the interband Rashba effect in symmetric double quantum wells. *Physical Review Applied*, **4**(3):034010, (2015).
- [38] R. J. Elliott. Theory of the effect of spin-orbit coupling on magnetic resonance in some semiconductors. *Physical Review*, **96**(2):266, (1954).
- [39] Y. Yafet. Calculation of the  $g$  factor of metallic sodium. *Physical Review*, **85**(3):478, (1952).
- [40] M. I. D'yakonov. Spin orientation of electrons associated with the interband absorption of light in semiconductors. *Soviet Journal of Experimental and Theoretical Physics*, **33**(5):1053, (1971).
- [41] Y. Lu, V. G. Truong, P. Renucci, M. Tran, H. Jaffrès, C. Deranlot, J. M. George, A. Lemaître, Y. Zheng, D. Demaille, P. H. Binh, T. Amand, and X. Marie. MgO thickness dependence of spin injection efficiency in spin-light emitting diodes. *Applied Physics Letters*, **93**(15):152102, (2008).
- [42] M. Holub and P. Bhattacharya. Spin-polarized light-emitting diodes and lasers. *Journal of Physics D: Applied Physics*, **40**(11):R179, (2007).
- [43] A. Fert and H. Jaffres. Conditions for efficient spin injection from a ferromagnetic metal into a semiconductor. *Physical Review B*, **64**(18):184420, (2001).
- [44] M. Kohda, Y. Ohno, K. Takamura, F. Matsukura, and H. Ohno. A spin Esaki diode. *Japanese Journal of Applied Physics*, **40**(12A):L1274, (2001).
- [45] X. Jiang, R. Wang, R. M. Shelby, R. M. Macfarlane, S. R. Bank, J. S. Harris, and S. S. P. Parkin. Highly spin-polarized room-temperature tunnel injector for semiconductor spintronics using MgO (100). *Physical Review Letters*, **94**(5):056601, (2005).
- [46] G. Salis, R. Wang, X. Jiang, R. M. Shelby, S. S. P. Parkin, S. R. Bank, and J. S. Harris. Temperature independence of the spin-injection efficiency of a MgO-based tunnel spin injector. *Applied Physics Letters*, **87**(26):262503, (2005).
- [47] G. Schmidt and L. W. Molenkamp. Electrical spin injection into semiconductors. *Physica E: Low-dimensional Systems and Nanostructures*, **9**(1):202, (2001).
- [48] B. T. Jonker, A. T. Hanbicki, Y. D. Park, G. Itskos, M. Furis, G. Kioseoglou, A. Petrou, and X. Wei. Quantifying electrical spin injection: Component-resolved electroluminescence from spin-polarized light-emitting diodes. *Applied Physics Letters*, **79**(19):3098, (2001).
- [49] D. P. DiVincenzo. Quantum computation. *Science*, **270**(5234):255, (1995).

- [50] R. Hanson, L. P. Kouwenhoven, J. R. Petta, S. Tarucha, and L. M. K. Vandersypen. Spins in few-electron quantum dots. *Reviews of Modern Physics*, **79**(4):1217, (2007).
- [51] R. Hanson, L. P. Kouwenhoven, J. R. Petta, S. Tarucha, and L. M. K. Vandersypen. Publisher’s note: Spins in few-electron quantum dots [rev. mod. phys. 79, 1217 (2007)]. *Reviews of Modern Physics*, **79**(4):1455, (2007).
- [52] H. A. Engel, L. P. Kouwenhoven, D. Loss, and C. M. Marcus. Controlling spin qubits in quantum dots. *Quantum Information Processing*, **3**(1-5):115, (2004).
- [53] J. M. Kikkawa and D. D. Awschalom. Resonant spin amplification in *n*-type GaAs. *Physical Review Letters*, **80**(19):4313, (1998).
- [54] L. Meier, G. Salis, I. Shorubalko, E. Gini, S. Schön, and K. Ensslin. Measurement of Rashba and Dresselhaus spin–orbit magnetic fields. *Nature Physics*, **3**(9):650, (2007).
- [55] E. Y. Tsymbal and I. Žutić. *Handbook of spin transport and magnetism*. CRC press, (2011).
- [56] F. Meier and B. P. Zakharchenya. *Optical Orientation*. North-Holland, (1984).
- [57] J. Frougier. *Toward Spin-LED and Spin-VECSEL operations at magnetic remanence*. PhD thesis, Université Paris Sud-Paris XI, (2014).
- [58] F. Meier and B. P. Zakharchenya. *Optical orientation*. Elsevier, (2012).
- [59] A. Takeuchi, K. Hosono, and G. Tatara. Diffusive versus local spin currents in dynamic spin pumping systems. *Physical Review B*, **81**(14):144405, (2010).
- [60] A. Brataas, Y. V. Nazarov, and G. E. W. Bauer. Finite-element theory of transport in ferromagnet–normal metal systems. *Physical Review Letters*, **84**(11):2481, (2000).
- [61] Y. Tserkovnyak, A. Brataas, and G. E. W. Bauer. Enhanced Gilbert damping in thin ferromagnetic films. *Physical Review Letters*, **88**(11):117601, (2002).
- [62] B. Heinrich, Y. Tserkovnyak, G. Woltersdorf, A. Brataas, R. Urban, and G. E. W. Bauer. Dynamic exchange coupling in magnetic bilayers. *Physical Review Letters*, **90**(18):187601, (2003).
- [63] T. Kimura, Y. Otani, and J. Hamrle. Enhancement of spin accumulation in a nonmagnetic layer by reducing junction size. *Physical Review B*, **73**(13):132405, (2006).
- [64] E. I. Rashba. Theory of electrical spin injection: Tunnel contacts as a solution of the conductivity mismatch problem. *Physical Review B*, **62**(24):R16267, (2000).

- [65] K. Ando, S. Takahashi, J. Ieda, H. Kurebayashi, T. Trypiniotis, C. H. W. Barnes, S. Maekawa, and E. Saitoh. Electrically tunable spin injector free from the impedance mismatch problem. *Nature Materials*, **10**(9):655, (2011).
- [66] O. Mosendz, J. E. Pearson, F. Y. Fradin, G. E. W. Bauer, S. D. Bader, and A. Hoffmann. Quantifying spin Hall angles from spin pumping: Experiments and theory. *Physical Review Letters*, **104**(4):046601, (2010).
- [67] A. K. Patra, S. Singh, B. Barin, Y. Lee, J. H. Ahn, E. del Barco, E. R. Mucciolo, and B. Özyilmaz. Dynamic spin injection into chemical vapor deposited graphene. *Applied Physics Letters*, **101**(16):162407, (2012).
- [68] Z. Y. Tang, E. Shikoh, H. Ago, K. Kawahara, Y. Ando, T. Shinjo, and M. Shiraishi. Dynamically generated pure spin current in single-layer graphene. *Physical Review B*, **87**(14):140401, (2013).
- [69] J. Sinova, S. O. Valenzuela, J. Wunderlich, C. H. Back, and T. Jungwirth. Spin Hall effects. *Reviews of Modern Physics*, **87**(4):1213, (2015).
- [70] N. Nagaosa, J. Sinova, S. Onoda, A. H. MacDonald, and N. P. Ong. Anomalous Hall effect. *Reviews of Modern Physics*, **82**(2):1539, (2010).
- [71] N. A. Sinitsyn. Semiclassical theories of the anomalous Hall effect. *Journal of Physics: Condensed Matter*, **20**(2):023201, (2007).
- [72] K. Ando and E. Saitoh. Spin Photodetector: Conversion of Light Polarization Information into Electric Voltage Using Inverse Spin Hall Effect. *Photodetectors*, page 405, (2012).
- [73] A. I. Ekimov and A. A. Onushchenko. Quantum size effect in three-dimensional microscopic semiconductor crystals. *Journal of Experimental and Theoretical Physics Letters*, **34**(6):345, (1981).
- [74] L. E. Brus. A simple model for the ionization potential, electron affinity, and aqueous redox potentials of small semiconductor crystallites. *The Journal of Chemical Physics*, **79**(11):5566, (1983).
- [75] B. L. Liang, Q. Yuan, L. L. Su, Y. Wang, Y. N. Guo, S. F. Wang, G. S. Fu, E. Marega, Y. I. Mazur, M. E. Ware, and G. Salamo. Correlation between photoluminescence and morphology for single layer self-assembled InGaAs/GaAs quantum dots. *Optics Express*, **26**(18):23107, (2018).
- [76] H. Drexler, D. Leonard, W. Hansen, J. P. Kotthaus, and P. M. Petroff. Spectroscopy of quantum levels in charge-tunable InGaAs quantum dots. *Physical Review Letters*, **73**(16):2252, (1994).
- [77] J. Y. Marzin, J. M. Gérard, A. Izraël, D. Barrier, and G. Bastard. Photoluminescence of single InAs quantum dots obtained by self-organized growth on GaAs. *Physical Review Letters*, **73**(5):716, (1994).

- [78] M. Paillard, X. Marie, P. Renucci, T. Amand, A. Jbeli, and J. M. Gérard. Spin relaxation quenching in semiconductor quantum dots. *Physical Review Letters*, **86**(8):1634, (2001).
- [79] P. Borri, W. Langbein, S. Schneider, U. Woggon, R. L. Sellin, D. Ouyang, and D. Bimberg. Ultralong dephasing time in InGaAs quantum dots. *Physical Review Letters*, **87**(15):157401, (2001).
- [80] M. Kroutvar, Y. Ducommun, D. Heiss, M. Bichler, D. Schuh, G. Abstreiter, and J. J. Finley. Optically programmable electron spin memory using semiconductor quantum dots. *Nature*, **432**(7013):81, (2004).
- [81] J. M. Elzerman, R. Hanson, L. H. Willems van Beveren, B. Witkamp, L. M. K. Vandersypen, and L. P. Kouwenhoven. Single-shot read-out of an individual electron spin in a quantum dot. *Nature*, **430**(6998):431, (2004).
- [82] L. Brus. Electronic wave functions in semiconductor clusters: experiment and theory. *The Journal of Physical Chemistry*, **90**(12):2555, (1986).
- [83] A. P. Alivisatos. Semiconductor clusters, nanocrystals, and quantum dots. *Science*, **271**(5251):933, (1996).
- [84] Y. Shirasaki, G. J. Supran, M. G. Bawendi, and V. Bulović. Emergence of colloidal quantum-dot light-emitting technologies. *Nature Photonics*, **7**(1):13, (2013).
- [85] Y. X. Yang, Y. Zheng, W. R. Cao, A. Titov, J. Hyvonen, J. R. Manders, J. G. Xue, P. H. Holloway, and L. Qian. High-efficiency light-emitting devices based on quantum dots with tailored nanostructures. *Nature Photonics*, **9**(4):259, (2015).
- [86] L. Qian, Y. Zheng, J. G. Xue, and P. H. Holloway. Stable and efficient quantum-dot light-emitting diodes based on solution-processed multilayer structures. *Nature Photonics*, **5**(9):543, (2011).
- [87] T. Kiba, X. J. Yang, T. Yamamura, Y. Kuno, A. Subagyo, K. Sueoka, and A. Murayama. Temperature dependence of the dynamics of optical spin injection in self-assembled InGaAs quantum dots. *Applied Physics Letters*, **103**(8):082405, (2013).
- [88] T. Yamamura, T. Kiba, X. J. Yang, J. Takayama, A. Subagyo, K. Sueoka, and A. Murayama. Growth-temperature dependence of optical spin-injection dynamics in self-assembled InGaAs quantum dots. *Journal of Applied Physics*, **116**(9):094309, (2014).
- [89] T. Amano, T. Sugaya, and K. Komori. Characteristics of 1.3  $\mu\text{m}$  quantum-dot lasers with high-density and high-uniformity quantum dots. *Applied Physics Letters*, **89**(17):171122, (2006).

- [90] A. Higo, T. Kiba, Y. Tamura, C. Thomas, J. Takayama, Y. Wang, H. Sodabanlu, M. Sugiyama, Y. Nakano, I. Yamashita, A. Murayama, and S. Samukawa. Light-emitting devices based on top-down fabricated GaAs quantum nanodisks. *Scientific Reports*, **5**:9371, (2015).
- [91] V. F. Motsnyi, P. Van Dorpe, W. Van Roy, E. Goovaerts, V. I. Safarov, G. Borghs, and J. De Boeck. Optical investigation of electrical spin injection into semiconductors. *Physical Review B*, **68**(24):245319, (2003).
- [92] O. M. J. Van't Erve, G. Kioseoglou, A. T. Hanbicki, C. H. Li, B. T. Jonker, R. Mallory, M. Yasar, and A. Petrou. Comparison of Fe/Schottky and Fe/AlO tunnel barrier contacts for electrical spin injection into GaAs. *Applied Physics Letters*, **84**(21):4334, (2004).
- [93] R. Fiederling, M. Keim, G. Reuscher, W. Ossau, G. Schmidt, A. Waag, and L. W. Molenkamp. Injection and detection of a spin-polarized current in a light-emitting diode. *Nature*, **402**(6763):787, (1999).
- [94] O. M. J. Van't Erve, G. Kioseoglou, A. T. Hanbicki, C. H. Li, and B. T. Jonker. Remanent electrical spin injection from Fe into AlGaAs/GaAs light emitting diodes. *Applied Physics Letters*, **89**(7):072505, (2006).
- [95] G. Itskos, E. Harbord, S. K. Clowes, E. Clarke, L. F. Cohen, P. Murray, R. Van Dorpe, and W. Van Roy. Oblique Hanle measurements of InAs/GaAs quantum dot spin-light emitting diodes. *Applied Physics Letters*, **88**(2):022113, (2006).
- [96] J. A. Gupta, D. D. Awschalom, X. Peng, and A. P. Alivisatos. Spin coherence in semiconductor quantum dots. *Physical Review B*, **59**(16):R10421, (1999).
- [97] R. J. Epstein, D. T. Fuchs, W. V. Schoenfeld, P. M. Petroff, and D. D. Awschalom. Hanle effect measurements of spin lifetimes in InAs self-assembled quantum dots. *Applied Physics Letters*, **78**(6):733, (2001).
- [98] K. Akahane, N. Yamamoto, and M. Tsuchiya. Highly stacked quantum-dot laser fabricated using a strain compensation technique. *Applied Physics Letters*, **93**(4):041121, (2008).
- [99] S. Hiura, K. Itabashi, K. Takeishi, J. Takayama, T. Kiba, and A. Murayama. Quantum spin transport to semiconductor quantum dots through superlattice. *Applied Physics Letters*, **114**(7):072406, (2019).
- [100] A. S. Bracker, E. A. Stinaff, D. Gammon, M. E. Ware, J. G. Tischler, A. Shabaev, Al. L. Efros, D. Park, D. Gershoni, V. L. Korenev, and I. A. Merkulov. Optical pumping of the electronic and nuclear spin of single charge-tunable quantum dots. *Physical Review Letters*, **94**(4):047402, (2005).

- [101] S. Grosse, J. H. H. Sandmann, G. Von Plessen, J. Feldmann, H. Lipsanen, M. Sopanen, J. Tulkki, and J. Ahopelto. Carrier relaxation dynamics in quantum dots: Scattering mechanisms and state-filling effects. *Physical Review B*, **55**(7):4473, (1997).
- [102] Y. Masumoto, S. Oguchi, B. Pal, and M. Ikezawa. Spin dephasing of doped electrons in charge-tunable InP quantum dots: Hanle-effect measurements. *Physical Review B*, **74**(20):205332, (2006).
- [103] Y. Chye, M. E. White, E. Johnston-Halperin, B. D. Gerardot, D. D. Awschalom, and P. M. Petroff. Spin injection from (Ga,Mn)As into InAs quantum dots. *Physical Review B*, **66**(20):201301, (2002).
- [104] C. H. Li, G. Kioseoglou, O. M. J. Van't Erve, M. E. Ware, D. Gammon, R. M. Stroud, B. T. Jonker, R. Mallory, M. Yasar, and A. Petrou. Electrical spin pumping of quantum dots at room temperature. *Applied Physics Letters*, **86**(13):132503, (2005).
- [105] S. Ghosh and P. Bhattacharya. Surface-emitting spin-polarized In<sub>0.4</sub>Ga<sub>0.6</sub>As/GaAs quantum-dot light-emitting diode. *Applied Physics Letters*, **80**(4):658, (2002).
- [106] Y. I. Mazur, V. G. Dorogan, E. Marega Jr, D. Guzun, M. E. Ware, Z. Y. Zhuchenko, G. G. Tarasov, C. Lienau, and G. J. Salamo. Effect of tunneling transfer on thermal redistribution of carriers in hybrid dot-well nanostructures. *Journal of Applied Physics*, **113**(3):034309, (2013).
- [107] C. Y. Jin, S. Ohta, M. Hopkinson, O. Kojima, T. Kita, and O. Wada. Temperature-dependent carrier tunneling for self-assembled InAs/GaAs quantum dots with a GaAsN quantum well injector. *Applied Physics Letters*, **96**(15):151104, (2010).
- [108] Y. I. Mazur, V. G. Dorogan, E. Marega Jr, Z. Y. Zhuchenko, M. E. Ware, M. Benamara, G. G. Tarasov, P. Vasa, C. Lienau, and G. J. Salamo. Tunneling-barrier controlled excitation transfer in hybrid quantum dot-quantum well nanostructures. *Journal of Applied Physics*, **108**(7):074316, (2010).
- [109] D. Guzun, Y. I. Mazur, V. G. Dorogan, M. E. Ware, E. Marega Jr, G. G. Tarasov, C. Lienau, and G. J. Salamo. Effect of resonant tunneling on exciton dynamics in coupled dot-well nanostructures. *Journal of Applied Physics*, **113**(15):154304, (2013).
- [110] K. Takeishi, S. Hiura, J. Takayama, K. Itabashi, M. Urabe, A. Washida, T. Kiba, and A. Murayama. Persistent high polarization of excited spin ensembles during light emission in semiconductor quantum-dot-well hybrid nanosystems. *Physical Review Applied*, **10**(3):034015, (2018).

- [111] X. J. Yang, T. Kiba, T. Yamamura, J. Takayama, A. Subagyo, K. Sueoka, and A. Murayama. Ultrafast spin tunneling and injection in coupled nanostructures of InGaAs quantum dots and quantum well. *Applied Physics Letters*, **104**(1):012406, (2014).
- [112] S. L. Chen, T. Kiba, X. J. Yang, J. Takayama, and A. Murayama. Power-dependent spin amplification in (In, Ga)As/GaAs quantum well via Pauli blocking by tunnel-coupled quantum dot ensembles. *Applied Physics Letters*, **108**(15):152103, (2016).
- [113] W. Rudno-Rudziński, D. Biegańska, J. Misiewicz, F. Lelarge, B. Rousseau, and G. Sek. Carrier diffusion as a measure of carrier/exciton transfer rate in InAs/InGaAsP/InP hybrid quantum dot–quantum well structures emitting at telecom spectral range. *Applied Physics Letters*, **112**(5):051103, (2018).
- [114] S. L. Chen, T. Kiba, X. J. Yang, J. Takayama, and A. Murayama. Temperature-dependent spin injection dynamics in InGaAs/GaAs quantum well-dot tunnel-coupled nanostructures. *Journal of Applied Physics*, **119**(11):115701, (2016).
- [115] Y. Puttisong, Y. Q. Huang, I. A. Buyanova, X. J. Yang, A. Subagyo, K. Sueoka, A. Murayama, and W. M. Chen. Anomalous spectral dependence of optical polarization and its impact on spin detection in InGaAs/GaAs quantum dots. *Applied Physics Letters*, **105**(13):132106, (2014).
- [116] S. Birner, T. Zibold, T. Andlauer, T. Kubis, M. Sabathil, A. Trellakis, and P. Vogl. Nextnano: General purpose 3-D simulations. *IEEE Transactions on Electron Devices*, **54**(9):2137, (2007).
- [117] C. Pryor. Eight-band calculations of strained InAs/GaAs quantum dots compared with one-, four-, and six-band approximations. *Physical Review B*, **57**(12):7190, (1998).
- [118] Y. Masumoto and T. Takagahara. *Semiconductor quantum dots: physics, spectroscopy and applications*. Springer Science & Business Media, (2013).
- [119] D. O’Connor. *Time-correlated single photon counting*. Academic Press, (2012).
- [120] W. Becker. *Advanced time-correlated single photon counting techniques*, volume **81**. Springer Science & Business Media, (2005).
- [121] S. Parola, M. Daanoune, A. Focsa, B. Semmache, E. Picard, A. Kaminski-Cachopo, M. Lemiti, and D. Blanc-Pélessier. Study of photoluminescence decay by time-correlated single photon counting for the determination of the minority-carrier lifetime in silicon. *Energy Procedia*, **55**:121, (2014).
- [122] S. Raymond, S. Fafard, P. J. Poole, A. Wojs, P. Hawrylak, S. Charbonneau, D. Leonard, R. Leon, P. M. Petroff, and J. L. Merz. State filling and time-resolved photoluminescence of excited states in  $\text{In}_x\text{Ga}_{1-x}\text{As}/\text{GaAs}$  self-assembled quantum dots. *Physical Review B*, **54**(16):11548, (1996).

- [123] W. M. Chen, I. A. Buyanova, K. Kayanuma, K. Nishibayashi, K. Seo, A. Murayama, Y. Oka, A. A. Toropov, A. V. Lebedev, S. V. Sorokin, and S. V. Ivanov. Identification of a dominant mechanism for optical spin injection from a diluted magnetic semiconductor: Spin-conserving energy transfer via localized excitations. *Physical Review B*, **72**(7):073206, (2005).
- [124] G. L. Bir, A. G. Aronov, and G. E. Pikus. Spin relaxation of electrons due to scattering by holes. *Soviet Journal of Experimental and Theoretical Physics*, **42**:705, (1976).
- [125] T. Kiba, T. Tanaka, Y. Tamura, A. Higo, C. Thomas, S. Samukawa, and A. Murayama. Impact of artificial lateral quantum confinement on exciton-spin relaxation in a two-dimensional gas electronic system. *AIP Advances*, **4**(10):107112, (2014).
- [126] X. M. Wen, L. V. Dao, P. Hannaford, S. Mokkaapati, H. H. Tan, and C. Jagadish. The state filling effect in *p*-doped InGaAs/GaAs quantum dots. *Journal of Physics: Condensed Matter*, **19**(38):386213, (2007).
- [127] T. Förster. Zwischenmolekulare energiewanderung und fluoreszenz. *Annalen der Physik*, **2**:55, (1948).
- [128] D. L. Dexter. A theory of sensitized luminescence in solids. *The Journal of Chemical Physics*, **21**(5):836, (1953).
- [129] S. K. Lyo. Energy transfer of excitons between quantum wells separated by a wide barrier. *Physical Review B*, **62**(20):13641, (2000).
- [130] S. Laurent, M. Senes, O. Krebs, V. K. Kalevich, B. Urbaszek, X. Marie, T. Amand, and P. Voisin. Negative circular polarization as a general property of *n*-doped self-assembled InAs/GaAs quantum dots under nonresonant optical excitation. *Physical Review B*, **73**(23):235302, (2006).
- [131] B. Pal, S. Y. Verbin, I. V Ignatiev, M. Ikezawa, and Y. Masumoto. Nuclear-spin effects in singly negatively charged InP quantum dots. *Physical Review B*, **75**(12):125322, (2007).
- [132] A. Shabaev, E. A. Stinaff, A. S. Bracker, D. Gammon, A. L. Efros, V. L. Korenev, and I. Merkulov. Optical pumping and negative luminescence polarization in charged GaAs quantum dots. *Physical Review B*, **79**(3):035322, (2009).
- [133] M. W. Taylor, E. Harbord, P. Spencer, E. Clarke, G. Slavcheva, and R. Murray. Optical spin-filtering effect in charged InAs/GaAs quantum dots. *Applied Physics Letters*, **97**(17):171907, (2010).
- [134] S. Hammersley, M. J. Kappers, F. C. P. Massabuau, S. L. Sahonta, P. Dawson, R. A. Oliver, and C. J. Humphreys. Effects of quantum well growth temperature on the recombination efficiency of InGaN/GaN multiple quantum wells

- that emit in the green and blue spectral regions. *Applied Physics Letters*, **107**(13):132106, (2015).
- [135] M. W. Taylor, P. Spencer, and R. Murray. Negative circular polarization as a universal property of quantum dots. *Applied Physics Letters*, **106**(12):122404, (2015).
- [136] S. Hiura, K. Takeishi, M. Urabe, K. Itabashi, J. Takayama, T. Kiba, K. Sueoka, and A. Murayama. Interdot spin transfer dynamics in laterally coupled excited spin ensemble of high-density InGaAs quantum dots. *Applied Physics Letters*, **113**(2):023104, (2018).
- [137] N. Liu, J. Tersoff, O. Baklenov, A. L. Holmes Jr, and C. K. Shih. Nonuniform composition profile in In<sub>0.5</sub>Ga<sub>0.5</sub>As alloy quantum dots. *Physical Review Letters*, **84**(2):334, (2000).
- [138] Y. Q. Huang, I. A. Buyanova, X. J. Yang, A. Murayama, and W. M. Chen. Effect of a phonon bottleneck on exciton and spin generation in self-assembled In<sub>1-x</sub>Ga<sub>x</sub>As quantum dots. *Physical Review Applied*, **9**(4):044037, (2018).
- [139] T. Inoshita and H. Sakaki. Electron relaxation in a quantum dot: Significance of multiphonon processes. *Physical Review B*, **46**(11):7260, (1992).
- [140] X. Q. Li, H. Nakayama, and Y. Arakawa. Phonon bottleneck in quantum dots: Role of lifetime of the confined optical phonons. *Physical Review B*, **59**(7):5069, (1999).
- [141] Y. I. Mazur, Z. M. Wang, G. J. Salamo, V. V. Strelchuk, V. P. Kladko, V. F. Machulin, M. Y. Valakh, and M. O. Manasreh. Investigation of indium distribution in InGaAs/ GaAs quantum dot stacks using high-resolution x-ray diffraction and Raman scattering. *Journal of Applied Physics*, **99**(2):023517, (2006).
- [142] T. B. Boykin, A. Ajoy, H. Ilatikhameneh, M. Povolotskyi, and G. Klimeck. Brillouin zone unfolding method for effective phonon spectra. *Physical Review B*, **90**(20):205214, (2014).
- [143] V. K. Kalevich, I. A. Merkulov, A. Y. Shiryaev, K. V. Kavokin, M. Ikezawa, T. Okuno, P. N. Brunkov, A. E. Zhukov, V. M. Ustinov, and Y. Masumoto. Optical spin polarization and exchange interaction in doubly charged InAs self-assembled quantum dots. *Physical Review B*, **72**(4):045325, (2005).
- [144] M. E. Ware, E. A. Stinaff, D. Gammon, M. F. Doty, A. S. Bracker, D. Gershoni, V. L. Korenev, Ș. C. Bădescu, Y. Lyanda-Geller, and T. L. Reinecke. Polarized fine structure in the photoluminescence excitation spectrum of a negatively charged quantum dot. *Physical Review Letters*, **95**(17):177403, (2005).

# Appendix A

## Publication

### A.1 Paper Publication

- “Electric field control of spin polarity in spin injection into InGaAs quantum dots from a tunnel-coupled quantum well” ,  
H. Chen, S. Hiura, J. Takayama, S. Park, K. Sueoka, A. Murayama,  
Applied Physics Letters 114, 133101:1-5 (2019).

### A.2 International conference

- “Electric-field-effect optical spin-injection device using *p*-doped InGaAs quantum dots” ,  
S. Park, H. Chen, J. Takayama, S. Hiura, and A. Murayama,  
7th International Workshop on Epitaxial Growth and Fundamental Properties of Semiconductor Nanostructures (Semicon Nano 2019), accepted for presentation, Sep. 24, 2019, Convention Hall of Integrated Research Center, Kobe University, Kobe, JAPAN.
- “Electric-field control of optical-spin injection from an InGaAs quantum well to *p*-doped quantum dots” ,  
S. Park, H. Chen, J. Takayama, S. Hiura, A. Murayama,  
Compound Semiconductor Week 2019 (CSW2019), May 20, 2019, Nara Kasugano International Forum, Nara, JAPAN.
- “Effects of electrical field on circularly polarized photoluminescence in InGaAs-based coupled nanostructures of quantum dots and a well” ,  
H. Chen, J. Takayama, S. Hiura, A. Subagy, K. Sueoka, A. Murayama,  
The 12th International Conference on Excitonic and Photonic Processes in Condensed Matter and Nano Materials (EXCON2018), PO120, July 12, 2018, Nara Kasugano International Forum, Nara, JAPAN.
- “Electric-field effects on spin polarity of In<sub>0.5</sub>Ga<sub>0.5</sub>As quantum dots after spin injection from In<sub>0.1</sub>Ga<sub>0.9</sub>As quantum wells” ,  
H. Chen, J. Takayama, S. Hiura, K. Sueoka, A. Murayama,

2nd JSPS workshop on Japan-Sweden frontiers in photon and spin functionalities of nanomaterials, O-5, October 24, 2018, Sekisuitei, Noboribetsu, JAPAN.

- **“Electric-Field Optical Device Controlling Electron-Spin Polarity of InGaAs Quantum Dots”**,

**H. Chen**, J. Takayama, S. Hiura, K. Sueoka, A. Murayama,

31st International Microprocesses and Nanotechnology Conference (MNC 2018), 16P-11-16, November 16, 2018, Sapporo Park Hotel, Sapporo, JAPAN.

### A.3 Domestic conference

- **” $p$  ドープ InGaAs 量子ドットへの電子スピン注入の電界制御”**,  
朴昭暎, 陳杭, 樋浦諭志, 高山純一, 村山明宏,  
第 80 回応用物理学会秋季学術講演会, 札幌, 日本, 2019/09.

- **”Electric-field control of spin transport property into InGaAs quantum dots from a tunnel-coupled quantum well”**,

**H. Chen**, J. Takayama, S. Hiura, K. Sueoka, and A. Murayama,

第 79 回応用物理学会秋季学術講演会, 名古屋, 日本, 2018/09.

- **”Effects of Electrical Field on Spin-related Optical Properties in InGaAs-based Coupled Nanostructures of Quantum Dots and Well”**,

**H. Chen**, H. D. Kim, J. Takayama, Y. Akei, S. Hiura, A. Subagyo, K. Sueoka, and A. Murayama,

第 78 回応用物理学会秋季学術講演会, 福岡, 日本, 2017/09.